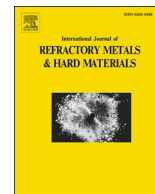




Contents lists available at ScienceDirect

International Journal of Refractory Metals and Hard Materials

journal homepage: www.elsevier.com/locate/IJRMHM

High-temperature wettability in hard materials: Comparison of systems with different binder/carbide phases and evaluation of C addition

M. de Nicolás-Morillas^{a,b,*}, L. Llanes^{c,d}, E. Gordo^a^a GTP – Department of Materials Science and Engineering, IAAB, Universidad Carlos III de Madrid, 28911 Leganés, Madrid, Spain^b INNANOMAT – Department of Materials Science and Metallurgical Engineering and Inorganic Chemistry, Escuela Técnica Superior de Ingeniería de Algeciras, Universidad de Cádiz, 11202 Algeciras Cádiz, Spain^c CIEFMA – Department of Materials Science and Engineering, Universitat Politècnica de Catalunya – BarcelonaTech, 08019 Barcelona, Spain^d Barcelona Research Center in Multiscale Science and Engineering, Universitat Politècnica de Catalunya – BarcelonaTech, 08019 Barcelona, Spain

ARTICLE INFO

Keywords:

Alternative hard materials
Metal-ceramic wettability
Contact-angle tests
Liquid phase sintering
High-temperature sintering
Powder metallurgy

ABSTRACT

Metal-ceramic wettability is a decisive parameter in the high-temperature sintering of hard materials. Wettability tests enable the study of this property with minimum material waste, especially useful in the search of alternative systems to WC-Co hardmetals. In this investigation, Fe-based binders – FeNiCr and FeCrAl – were tested on Ti(C, N) and WC substrates, aiming to assess: the high-temperature interactions, the dissolutive character of the liquid phase and the nature of the interphases generated, and the influence on sintering behaviour. As a result, FeNiCr led to excellent wetting scenarios for both ceramics, whereas FeCrAl alloys induced the formation of aluminium oxides. The effect of C addition on wettability was also evaluated, resulting in an improvement of this property by the inclusion of this element in the binder phase. Inspection of the microstructures resultant from powder metallurgy processing of the different configurations confirmed their excellent correlation with wettability results. As a consequence, the effectivity of this technique as a model of the sintering scenario could be asserted.

1. Introduction

WC-Co hardmetals have been strongly rooted to the industry due to its outstanding properties, especially regarding hardness and toughness, two valuable properties in the niche of cutting tools [1]. However, the relatively recent inclusion of W and Co in European and American critical raw materials [2] and toxicity – REACH [3] and NTP [4,5] – lists have driven the study of alternative materials. In this sense, there exist two approaches: the partial or total substitution of Co, and seeking for a WC competitor as ceramic phase [6–8].

With respect to the binder phase, Fe-based alloys have proven to be excellent candidates as Co substitutes. Fe has a relatively low price – about 700 USD/T (steel) compared to 70,000 USD/T for Co [9] –, is non-toxic and can be heat-treated to adjust the material final properties for the desired application [10–12]. Furthermore, its inclusion as a binder element in WC-based materials has resulted in enhanced mechanical properties [13]. The addition of alloying elements, such as Cr, Ni or Al, has also demonstrated to improve oxidation [14–17] and corrosion [13,15,18–29] resistance of these materials, among other properties. Concerning the substitution of the ceramic phase, titanium carbonitride

– Ti(C,N) – cermets, have arisen as very promising options, on the basis of providing advantages like high wear resistance or chemical stability [30]. The combination of both strategies implies a challenge – primarily based on the poor wettability demonstrated by Fe-Ti(C,N) system –, but also the most sustainable alternative. Hard materials are manufactured following a Powder Metallurgy (PM) route, which entails the blending of metal-ceramic powders, pressing of the mixtures into green parts and their subsequent sintering to attain the final samples. Regarding the sintering stage, these composites are commonly and commercially shaped by Liquid Phase Sintering (LPS). During this processing stage, the binder transforms into a liquid and the wetting behaviour is essential during this procedure and microstructural development. Porosity removal, solution-precipitation and final densification also occur during LPS [31].

Regarding the combination of both substitutional strategies, Ti(C,N)-Fe15Ni cermets have attained dense samples with a homogeneous microstructure, evidencing the excellent metal-ceramic wettability attained by Ni addition [32]. Moreover, the development of a core-rim structure in the carbide has been avoided, thus approaching the biphasic configuration of hardmetals [32,33]. Continuing with this

* Corresponding author.

E-mail address: mnicolas@ing.uc3m.es (M. de Nicolás-Morillas).<https://doi.org/10.1016/j.ijrmhm.2022.106081>

Received 14 September 2022; Received in revised form 28 November 2022; Accepted 7 December 2022

Available online 9 December 2022

0263-4368/© 2022 The Authors. Published by Elsevier Ltd. This is an open access article under the CC BY-NC-ND license (<http://creativecommons.org/licenses/by-nc-nd/4.0/>).

investigation line, the authors of this study proposed a flexible and systematic methodology to ease the task of designing and producing alternative hard materials [34]. It consists of three sequential steps, where the tools for thermodynamic simulation, validation and experimental processing are integrated, as follows:

- **Step 1: Thermodynamic simulation of phase diagrams.** It involves calculation of metal-alloy phase diagrams and their combination with predominant ceramic phases by means of the CALculation of PHase Diagrams (CALPHAD) method. The inclusion of new alloying elements – Cr and Al – and different compositions were evaluated, comparing the roles of WC and Ti(C,N). Compositions that fulfilled certain prescribed criteria were selected for further study.
- **Step 2: Validation of thermodynamic simulation.** It allows to assess the effectiveness of the simulation step.
- **Step 3: Processing of hard materials.** It includes manufacturing of various metal-ceramic combinations by PM following different routes, until achieving an optimum balance of microstructural and mechanical properties.

Focusing on the second step, validation of the simulation was performed by means of three different experimental techniques: Differential Thermal Analysis-Thermogravimetry-Mass Spectroscopy (DTA-TG-MS), X-Ray Diffraction (XRD) at room and high temperature (RT and HT, respectively), and high-temperature wettability tests. The main purposes were (1) to check the predicted-experimental validity of phases and transformation temperatures, and (2) to evaluate the interaction at high temperature between metallic and ceramic phases. Concerning the assessment of wetting behaviour, wettability or contact angle tests were performed as a model of the metal-ceramic interaction at high temperature. It is a cost-effective technique – in terms of material use – that enables to assess the sinterability of a specific metallic binder-ceramic phase system, as well as to study scenarios of different modifications that may be needed. In doing so, a liquid promoter – bulk of the metal binder – is placed on top of a solid – ceramic substrate. When temperature is raised and a droplet forms, the contact angle between the surface of the liquid and that of the solid can be measured, either by an adapted camera to the equipment or after cooling by transversal characterisation. The value of this contact angle (θ) is determined by the superficial tension of each phase taking part in the test – liquid, solid and vapour –, as defined by Young in the 19th century and collected in Eq. (1), where γ_{sv} , γ_{sl} and γ_{lv} are the solid-vapour, solid-liquid and liquid-vapour surface tensions, also represented in Fig. 1:

$$\gamma_{sv} - \gamma_{sl} = \gamma_{lv} \cos\theta \quad (1)$$

There are three possible scenarios that can develop once the liquid – the metal – and the solid – the ceramic – are in contact: inert, reactive or dissolutive. Inert or static systems describe no reaction between the liquid and the solid. They show the actual wettability between the two phases, i.e., the one that depends exclusively on their initial physico-chemical characteristics. Reactive systems are dynamic and take place when the liquid reacts with the solid, resulting in the formation of a new phase. Dissolutive systems are also of dynamic type and entail dissolution of the solid by the liquid phase. Wettability will be strongly

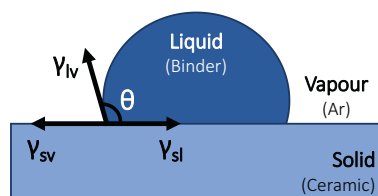


Fig. 1. Sketch of the equilibrium in the surface tension among the three phases – liquid (binder phase), solid (ceramic phase) and vapour (Ar) – involved in a contact angle test [55].

governed by the effect impinged dynamically, either by the formation of a new phase or by the modification of the metal composition by solution-precipitation of the ceramic phase, leading to the variation of the surface energy of the liquid. Both wettability and solubility are key for a good metal-ceramic bonding and microstructure [32,35–37]. Previous contributions on this topic in the hard material field have shed paramount worth-noting light, and a brief review of them is now presented.

Differences among TiC and TiN, the constituents of Ti(C,N) were investigated by Alvaredo et al. [32]. They assess the wetting scenario of Fe-TiC and Fe-TiN by contact-angle testing. It was evidenced that Fe-TiN led to an inert system, with a high angle value ($\theta = 93^\circ$) that does not evolve throughout time. On the other hand, TiC-Fe wetting experiment showed a high initial contact angle ($\theta > 90^\circ$) that decreases as a function of time. At the end of the test, an angle value of 3° could be measured. Moreover, scanning electron microscopy (SEM) characterisation of its interface revealed dissolution of TiC particles and metal infiltration into the substrate, yielding a composite structure. Testing of Fe-Ti(C,N) unveiled a combined TiN-TiC behaviour. Thus, a final contact angle of 60° was measured, and interfacial characterisation revealed a narrow composite region – $10 \mu\text{m}$ – where Ti(C,N) and Fe coexisted. Nevertheless, as commented before, the lack of wettability between Fe and Ti (C,N) can be improved by the addition of alloying elements, a field where Ni stands out as an excellent choice. This study indicated that Ni-Ti(C,N) assembly derived in a final contact angle of 10° and penetration into the ceramic substrate, giving sign of excellent wettability and binder-ceramic relation. As a consequence, inclusion of a 15 wt% of this element in the Fe-based bulk resulted in a synergy between both Fe/Ni-Ti(C,N) scenarios. An angle value $\theta = 24^\circ$ was measured and combined dissolution-infiltration of the alloy in the substrate was discerned in a region of $>100 \mu\text{m}$ wide. Another way of upgrading Fe-Ti(C,N) wettability is by the addition of secondary carbides, such as Mo_2C and WC. This enhancement was also confirmed by Alvaredo et al. with the performance of contact angle studies, where wettability improvement was evidenced by a decrease in the angle value. Carbide addition may either modify the solid-liquid surface tension or affect binder-carbide solubility [38–40].

Another relevant high-temperature wettability work in the hard-metal field, employing WC as ceramic phase, is the one carried out by Konyashin and co-workers [41]. In this study, contact angles of Co on a WC substrate were assessed, corresponding to different C contents. Very interesting, wettability was impaired by C addition. Although melting of the metal occurred earlier with increasing C content, a slower spreading of liquid Co on the WC surface was observed. Hence, a higher angle value was measured after cooling. Moreover, these findings were related to carbide coarsening and sharp-edged morphology for sintered composites with high C inclusion. An additional and remarkable work involving WC is the one conducted by Silva et al. [42], where contact angles of Cu-WC and Co-WC surfaces were evaluated, evidencing the improved wettability in the latter. Furthermore, effectiveness of WC-Co sputtered with WC as a recreation model of WC substrates was also assessed. From the perspective of the ceramic phase used in these studies, it is worth to highlight that in the present research work, the influence of C on metal-ceramic wettability has been assessed in Ti(C,N)-based systems – i.e., using Ti(C,N) substrates. To the best knowledge of the authors, there is not any study addressing such systems in the literature to date.

In this work the evolution of novel Fe-based alloy compositions (metallic phase) as temperature was elevated on two different ceramic substrates - Ti(C,N) and WC - was recorded. In doing so, sintered bulks of two pre-designed metallic compositions – FeNiCr and FeCrAl – were placed on top of the referred ceramics. The study of the metal droplet evolution, as well as the transversal characterisation of the assembly after the completion of the test – for those samples that showed metal-ceramic adherence –, served to predict the sintering-stage effectiveness of the different hard material configurations. As a result, FeNiCr evidenced excellent interaction with dissimilar wetting scenarios when

combined with each ceramic phase. On the other hand, FeCrAl alloy led to oxidation and hindering of wettability. These setups could also be evidenced and confirmed by inspecting the microstructure of the hard materials, obtained by processing each composition following a PM route.

2. Experimental procedure

Thermodynamic simulation was conducted with the purpose of designing binder and hard material compositions. In doing so, ThermoCalc® software was used. Databases TCFE7 and TCFE9, developed for steels and Fe-alloys, were employed to simulate binder and composite phase diagrams. Effectiveness of the method and databases employed was confirmed by reproducing standardised WC-Co diagrams (Refs. [12, 15, 43]), obtaining the exact same results.

Once the binder and metal-ceramic combinations were designed, high-temperature wetting experiments were conducted. They are of great importance to understand the high-temperature behaviour between the two main phases, during LPS process, in the materials studied. The tests were carried out to melt the metallic phase and measure the contact angle of the molten metal on the ceramic phase [32,40,41]. This value is governed by surface tensions of the liquid metal binder, gas (Ar, in the present case) and ceramic substrate.

As there are not any standards for high-temperature experiments, the procedures defined for low temperatures were followed [44,45]. Sessile drop technique was used [40,46] to measure the contact angle, as explained and depicted in Fig. 1. It was done by means of recording the formation and evolution of a metal drop on the surface of a solid substrate through pictures and videos. In doing so, a metal bulk (40–70 mg) was placed on top of a binderless ceramic substrate and inserted in a tubular furnace with an inert atmosphere. As temperature was risen, a camera recorded the formation and evolution of the metal drop. The equipment used to conduct this test was Drop Shape Analysis for High Temperatures (DSAHT), from Krüss (Germany). A schematic illustration of the furnace and sample assembly is shown in Fig. 2.

Metal bulk was manufactured by first mixing elemental powders in a Turbula® for 4 h. Elemental and prealloyed powders were used. The former were Fe (BASF, purity: 99.5%), Ni (CNPC Powder, purity: 99.8%), Cr (Skyspring nanomaterials, purity: 99.5%) and Al (Skyspring nanomaterials, purity: >99.0%), and had a maximum D50 of 5 µm. The objective of selecting powders with such a low particle size was to promote their mixing and dispersion during the milling step. The pre-alloy powder was Fe16Cr3Al, provided by Goodfellow (United Kingdom) and had a maximum particle size of 45 µm. All metal powders were gas atomised. After mixing, they were pressed uniaxially at 600 MPa and sintered in a high-vacuum furnace (10^{-5} mbar) at 1450 °C for 1 h. This allowed the diffusion of elements and formation of the alloys, according to each composition.

Binderless Ti(C,N) substrates were produced by Spark Plasma Sintering (SPS) at Institute of Ceramic and Glass (ICV-CSIC, Spain). They were sintered at 1900 °C (100 °C/min) and 70 MPa with DR SINTER SPS-1050-CE Fuji Electronic Industrial (Japan) equipment, achieving a relative density of 99.5%. Binderless WC substrates were provided by Fraunhofer-Gesellschaft Institute (Germany). To conduct the contact-angle test, surface of substrates was ground and polished with diamond paste down to 1 µm, to attain a smooth surface with no

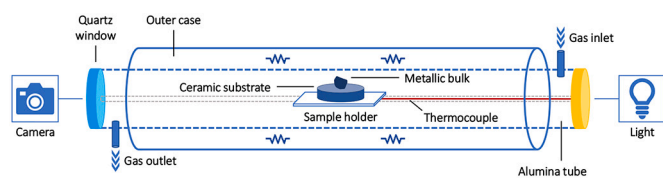


Fig. 2. Schematic illustration of the contact angle furnace and sample assembly, adapted from Ref. [32].

irregularities that could influence the final result.

Before starting the test, the air inside the furnace tube was purged up to five times with Ar (purity: 99.999%) and a vacuum pump. A constant Ar flow was maintained throughout the experiment, ensuring the presence of an inert atmosphere. Fig. 3 details the heating cycle used in these tests. First, temperature was manually risen up to 300 °C, to promote temperature stabilisation and a correct matching between the software and thermocouple temperature values. Then, the programmed cycle was used, where different heating ramps were set to ensure a correct recording of the drop formation and evolution. A final temperature of 1500/1600–1650 °C – depending on the binder and substrate composition – was achieved, after which the sample was cooled to RT under Ar flow, to avoid oxidation during the cooling stage.

After cooling, the samples where a metal drop was formed, and a metal/ceramic assembly was achieved, were cut transversally and embedded in conductive resin. Their cross sections were prepared by a conventional metallographic route, which entailed grinding and polishing with diamond paste down to 1 µm. They were characterised in terms of their microstructure and composition, using a combination of Field-Emission Scanning Electron Microscopy (FESEM) and Energy Dispersive X-Ray (EDX), with the performance of mappings. FEI Teneo (Philips, Netherlands) equipment was used.

Table 1 summarises the ceramic-metal combinations tested in this study. Regarding the comparison of binder phases, two different alloys were investigated: FeNiCr and FeCrAl. It should be noted that two FeCrAl compositions were studied: Fe15Cr10Al – using elemental powders, and Fe16Cr3Al – employing a prealloyed powder provided by Goodfellow (United Kingdom). Results were also contrasted with the ones obtained in a previous investigation with an Fe15Ni binder [32]. Moreover, the addition of extra C to the FeNiCr alloy when combined with Ti(C,N) was also studied. It is worth pointing out that C was added as graphite to the binder elemental powders before their mixing, and its percentage is indicated with respect to the metal phase.

As a proof of concept, hard material microstructures with different binder and carbide compositions were prepared to correlate the sintering behaviour with the wetting ability. In doing so, FESEM-EDX techniques were used.

Discussion of the results obtained for C-addition samples was completed with DTA-TG-MS analyses. These tests were employed to check solidus and liquidus temperatures of the metal-ceramic system, both already estimated in the simulation step and observed during the wetting tests. Setaram Setsys Evolution (France) equipment was used. Samples, with a mass of 60–80 mg, were placed inside an alumina (Al_2O_3) crucible and heated up to 1600 °C at 20 °C/min. A pure Ar atmosphere was used (99.999%), with a flow of 40 ml/min to avoid oxidation and the distortion of the results.

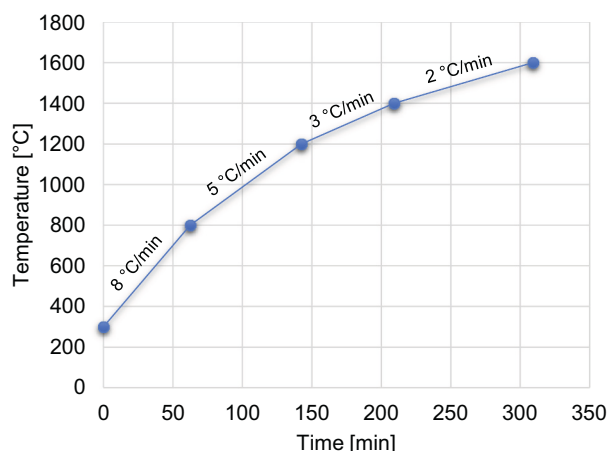


Fig. 3. Programmed heating cycle for the contact angle test.

Table 1
Summary of the wettability experiments performed.

| Phase under study | Ceramic phase | Metal phase | Type of metal powders | C addition* [wt%] |
|------------------------|---------------|-------------|-----------------------|-------------------|
| Wettability on Ti(C,N) | Ti(C,N) | Fe15Ni10Cr | Elemental | 0 |
| | | Fe15Ni10Cr | | 1 |
| | | Fe15Cr10Al | Prealloy | 0 |
| | | Fe16Cr3Al | | 0 |
| Wettability on WC | WC | Fe15Ni10Cr | Elemental | 0 |
| | | Fe15Cr10Al | Prealloy | |
| | | Fe16Cr3Al | | |

* C added to the metal phase.

It is worth mentioning that for Ti(C,N)-Fe15Ni10Cr contact angle using no C addition, Atomic Force Microscopy (AFM) and nano-indentation techniques were also implemented. Results of this system and analyses can be consulted in Ref. [34].

In the case of WC samples, with the aim of reliable distinction of phases present as well as of possible porosity, the active layers of the back-scattered electron detector (CBS) of FEI Teneo FESEM were modified. CBS uses concentric segmentation of the detector diode to distinguish between backscattered electrons close to the beam axis (inner segment, preferentially composite contrast) and those scattered far from the beam axis (outer segment, more topographical signal). Fig. 4 shows a schematic illustration of the CBS detector layers, labelled as A, B, C and D, from inner to outermost ones.

As an illustrative example, Fig. 5 shows the microstructure of a WC-Fe15Ni10Cr sample using the cited combinations of detectors/modes in FEI Teneo FESEM:

Figure 5 (a) 'CBS' (BSE) detector and 'All' mode, where all the layers are active. It refers to the normal BSE image with suppressed topographical contrast and maximum atomic number contrast.

Figure 5 (b) 'CBS' (BSE) detector and 'A+B-C-D' mode. The obtained image is pseudo-topographical, with suppressed atomic number contrast and maximum topographical contrast. In this way, the final picture is a negative of the former image with all the detector layers activated. As it can be appreciated, this last micrograph shows the same type of colours and contrast as with a Ti(C,N)-based sample – Ti(C,N)-Fe15Ni10Cr – using CBS/All mode, as seen in Fig. 5 (c).

3. Results and discussion

A summary of the results obtained for all metal-ceramic combinations studied in this investigation is displayed in Table 2. This *Results and discussion* section will be divided into the two types of ceramic substrates employed, as indicated previously in Table 1: wettability on Ti(C,N) and

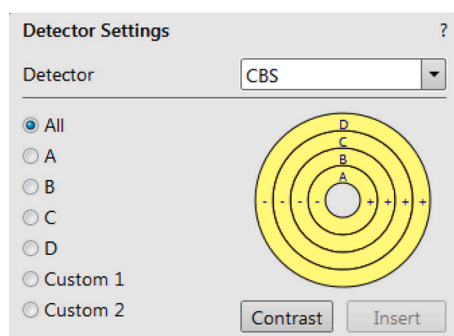


Fig. 4. FEI Teneo software setting for CBS detector, showing the layers into which it is divided: A, B, C and D. In the picture, all the layers are activated (CBS/All).

wettability on WC.

3.1. Wettability on Ti(C,N)

This part will be devoted to present and discuss the results attained from the tests performed on Ti(C,N) substrates, focusing on the role played by each studied metal alloy, i.e., FeNiCr and FeCrAl, the latter using elemental and prealloyed powders. Effect of C addition on wettability will be also addressed and investigated in FeNiCr alloy.

3.1.1. Ti(C,N)-FeNiCr

Chromium was added in a 10 wt% to Fe15Ni alloy, whose high-temperature wetting behaviour was assessed on a Ti(C,N) substrate in Ref. [34], using no C addition. As evidenced in the cited investigation and can also be appreciated in Table 2, a metallic droplet was formed and a final angle value of 26° could be measured. This result confirmed a satisfactory wetting behaviour, accompanied by dissolution of Ti(C,N) particles, penetration of the binder into the ceramic substrate – measuring a layer of $336 \pm 16 \mu\text{m}$ –, and carbide reprecipitation at the metal drop region. These reprecipitated carbides corresponded to TiC and $\text{M}_{23}\text{C}_6/\text{M}_7\text{C}_3$. The two-phase metal/ceramic region, formed between the metal-drop and Ti(C,N)-substrate single phases, resembles the two-phase microstructure obtained after sintering. It should be noted that the carbide-dissolving ability of the metal binder was observed in wettability studies carried out for a Ti(C,N)-Fe15Ni system [32], obtaining similar contact angle values and microstructure of the metallic-ceramic interface. This is the desirable situation according to German et al. [31] for a densification situation, where the liquid metal dissolves the grain boundaries of Ti(C,N) and solidifies upon cooling.

Mapping analyses were performed in this study at 15 kV, repeating the ones carried out in a previous contribution by the authors [34], which was conducted at 12 kV. Results are displayed in Fig. 6. This time, Ti(C,N) phase appears in blue and binder phase can be seen in red. Moreover, a third phase could be spotted, coloured in yellow. This new region surrounded the ceramic particles at the substrate area and the secondary carbide that reprecipitated in the metal zone. Its composition, enriched in Cr, Ti and C suggests that it entails a small interphase between the ceramic and metallic phases, with inclusion of elements from both (preferentially from the binder).

As a proof of concept, the microstructure of Ti(C,N)-FeNiCr system, obtained after processing by PM, is shown in Fig. 7. A homogeneous microstructure, with optimum carbide dispersion, can be appreciated. This correlates with the excellent metal-ceramic interaction observed at the contact angle test, given in terms of contact angle value and microstructure of the two-phase metal/ceramic region.

The role of C addition. Aiming to study the effect of C addition in Fe15Ni10Cr binder, DTA-TG technique was implemented. These tests were carried out to blended-powder agglomerates (green samples) and sintered-alloy bulks, with and without C addition, to validate liquid phase formation simulated by Thermo-Calc® with respect to C content. Fig. 8 shows a correlation between the predicted solidus/liquidus temperatures and the ones experimentally obtained by means of DTA-TG for the studied alloy, also detailed in Table 3. Endothermic peaks in the DTA plot indicate liquid phase formation. Onset and maximum melting temperatures – T_{ONSET} and T_{MAX} , respectively – were calculated as depicted in the DTA graph, i.e., at the points where tangents to the curve crossed each other. They can be related to Thermo-Calc® (TC) solidus and liquidus temperatures, and relative comparison then being taken as validating action of the phase diagram [34]. Onset temperature may be linked to the solidus one, as this is the region where liquid phase starts to appear, coexisting with some solid phase remaining in the binder. Similarly, maximum and liquidus temperatures are comparable, as they indicate the state where the binder phase has completely transformed into liquid. As it can be observed, for 0 wt% C, both solidus and liquidus

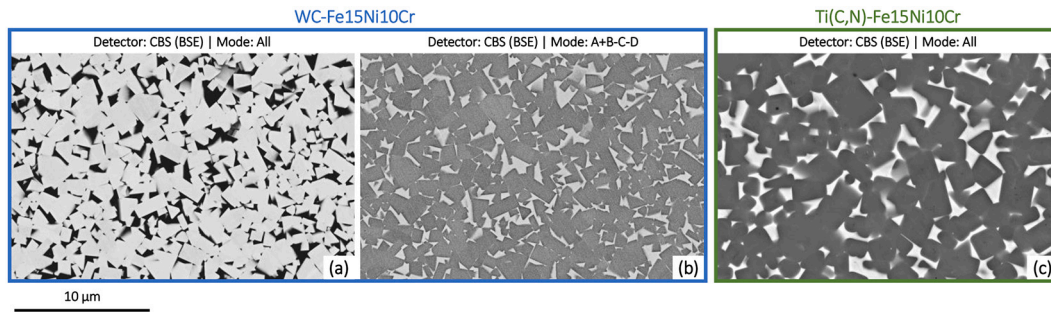


Fig. 5. FESEM micrographs of a WC-based hard material (WC-Fe15Ni10Cr) using the two combinations of detectors/modes: (a) CBS/All and (b) CBS/A+B-C-D. (c) Ti (C,N)-Fe15Ni10Cr micrograph using CBS/All mode and showing the same type of contrast as CBS/A+B-C-D for WC-Fe15Ni10Cr.

Table 2

Summary of results on contact angle evolution for all the wettability tests performed in this study.

| Ceramic substrate | Metal alloy | Contact angle evolution | | | |
|-------------------|---------------------------|-------------------------|---|---------|---------|
| Ti(C,N) | Fe15Ni10Cr-0C (Elemental) | 1440 °C | 1523 °C | 1546 °C | 1590 °C |
| | Fe15Ni10Cr-1C (Elemental) | 63 °C | 1431 °C | 1483 °C | 1516 °C |
| | Fe15Cr10Al-0C (Elemental) | 1419 °C | 1554 °C | 1597 °C | 1650 °C |
| | Fe16Cr3Al-0C (Prealloy) | 1419 °C | 1554 °C | 1597 °C | 1650 °C |
| | Fe15Ni10Cr-0C (Elemental) | 300 °C | 1405 °C | 1418 °C | 1500 °C |
| | Fe15Cr10Al-0C (Elemental) | 1400 °C | 1550 °C | 1600 °C | 1650 °C |
| | Fe16Cr3Al-0C (Prealloy) * | 185 °C | 551 °C | 1511 °C | 1650 °C |
| | | | * Liquid phase and crater formation are indicated in light blue and orange, respectively. | | |

temperatures virtually coincide in the phase diagram, indicated by the label NC. Meanwhile, as C content increases, so does the simulated range between $T_{solidus}$ and $T_{liquidus}$. At 1 wt% C, solidus and liquidus points are labelled as C_L and C_S respectively.

Several conclusions can be extracted from these results:

- First, although simulation predicted compositions without C to exhibit equal values for $T_{solidus}$ and $T_{liquidus}$ (NC), experimental analyses revealed that both compositions had different T_{ONSET} and

T_{MAX} ($T_{ONSET} < T_{MAX}$), for both their powder agglomerate and sintered bulk configurations.

- C addition induced an increase in the radius of the onset curve, as compared to the sintered bulk without C. It implies a more gradual transition to the liquid state, in agreement with the wider range between solidus (C_S) and liquidus (C_L) temperatures, i.e., region $L+\gamma$, observed in the diagram.

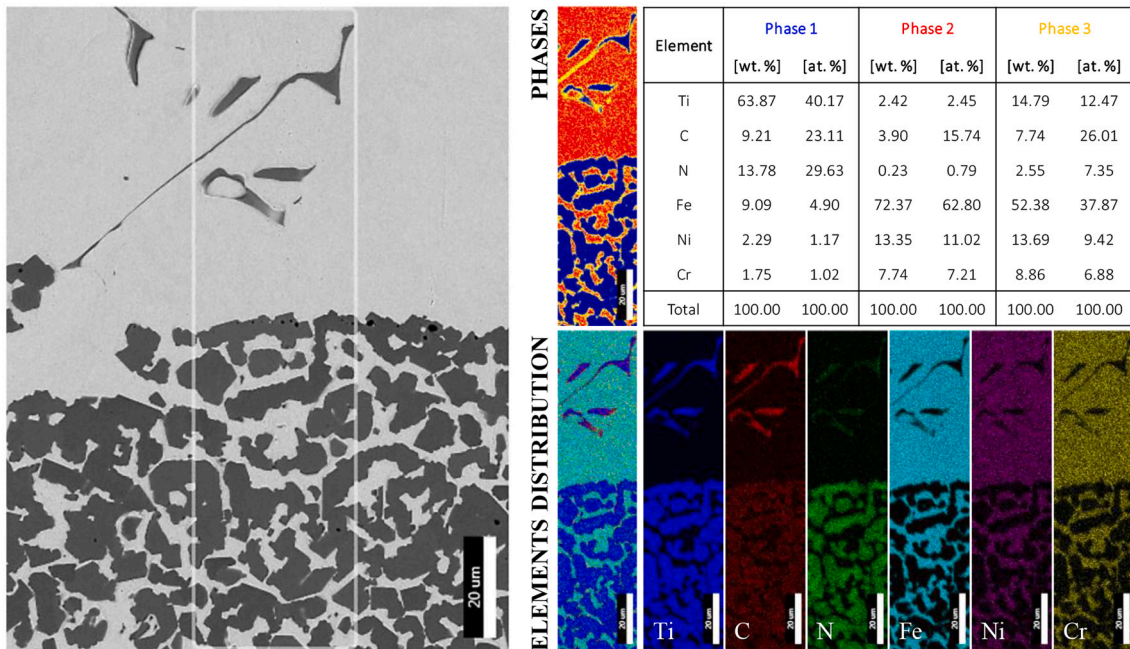


Fig. 6. Repetition of mapping analysis (Ref. [34]) of TiCN-Fe15Ni10Cr (0 wt% C) metal/ceramic region at 15 kV.

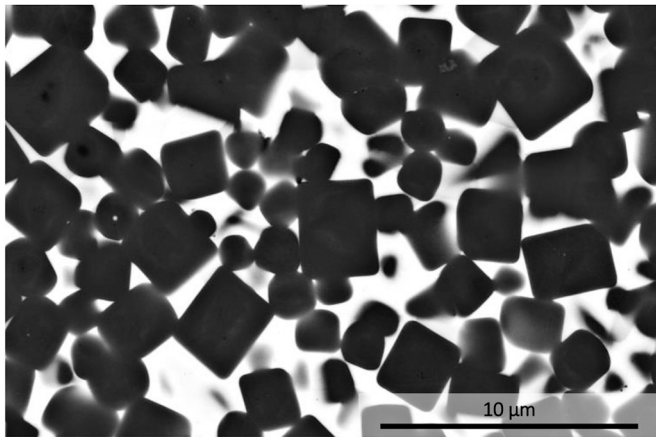


Fig. 7. FESEM image (x5000, CBS) of Ti(C,N)-Fe15Ni10Cr microstructure, processed by powder metallurgy (attritor milling + SHIP) and using no C addition.

SHIP = Sinter-Hot Isostatic Pressing.

- C addition led to a displacement of T_{MAX} towards lower temperature values, a well-known effect of C [8,51]. This is also in total consonance with TC predictions.
- Liquidus temperatures of powder-blend and sintered-bulk coincide for 0 wt% C. This result may indicate maintenance of nominal content of the elements after sintering. Nevertheless, these experimental liquidus temperatures are higher than the ones predicted by ThermoCalc®. This variation becomes more significant when C is added to the alloy, showing that the prediction is more accurate when no extra C is included. This phenomenon may be due to C loss as the material is heated, as also observed during the sintering of hard materials.
- It can be noticed that, after the sintering, oxidation is avoided, as shown by the TG curves for powder agglomerate and sintered bulk at 0 wt% C addition. The raw powder agglomerate gains mass, corresponding to oxygen acquired in the heating stage. Contrarily, the sintered bulk does not experience this mass increment, as the solid-solution alloy tends to be more chemically stable and less reactive.

Then, influence of C addition on wettability was assessed by means of contact-angle testing. In doing so, Fe15Ni10Cr – adding 1 wt% C to the metal phase – and a Ti(C,N) substrate were employed. Table 2 shows sequential images of the drop formation and evolution, captured by the camera adapted to the equipment. Four temperatures are shown: 63 °C (at the beginning of the test), 1431 °C, 1483 °C and 1516 °C. In this case, changes in the bulk shape started to be appreciable from 1300 °C on. At 1431 °C, the T_{ONSET} value from DTA test, bulk configuration evolved to the state that can be seen in the image. As temperature was risen, a drop effectively formed, which took place at approximately 1478 °C. Thus, addition of C translated into an earlier drop formation with respect to the C-free composition, which occurred at 1523 °C approximately. Heating was continued until reaching 1600 °C, where a final contact angle of 14° could be measured in the images of the adapted camera. This result evidences an improved wettability with respect to the system without C, where the contact angle value was 26° [34].

Moreover, droplet had already flattened at 1516 °C, showing a different evolution from that evidenced for the Ti(C,N)-Fe15Ni10Cr system with no C addition [34]. This could be characterised quantitatively by representing the contact angle value as a function of temperature for both compositions (Fig. 9). As it can be appreciated, addition of C promotes not only the decrease of the contact angle to lower temperatures but also achievement of a lower final value, as stated before.

After cooling, the resultant assembly was cut transversally, and the cross section was characterised by FESEM and EDX. Fig. 10 shows two FESEM images of (a) the metal drop profile and (b) the metal penetration layer into Ti(C,N) substrate. As it can be seen, there is a greater dissolutive capacity of the metal phase and penetration into the ceramic substrate, as compared to the assembly with no extra C. As a result, a diffusion layer of $636 \pm 7 \mu\text{m}$, almost 100% deeper than without C addition, is attained.

Fig. 11 shows a mapping analysis (15 kV) of the metal-ceramic region, where the phases and elements distribution can be observed. As with the analysis of TiCN-FeNiCr-0C sample at 15 kV (Fig. 6), three phases were spotted: Phase 1 (red), involving Ti(C,N) particles and secondary carbides reprecipitated in the metal region; Phase 2 (blue), corresponding to the metallic binder; and Phase 3 (yellow), an inter-phase that surrounds carbide particles. In the element-distribution analysis, the same pattern as with Ti(C,N)-Fe15Ni10Cr without C

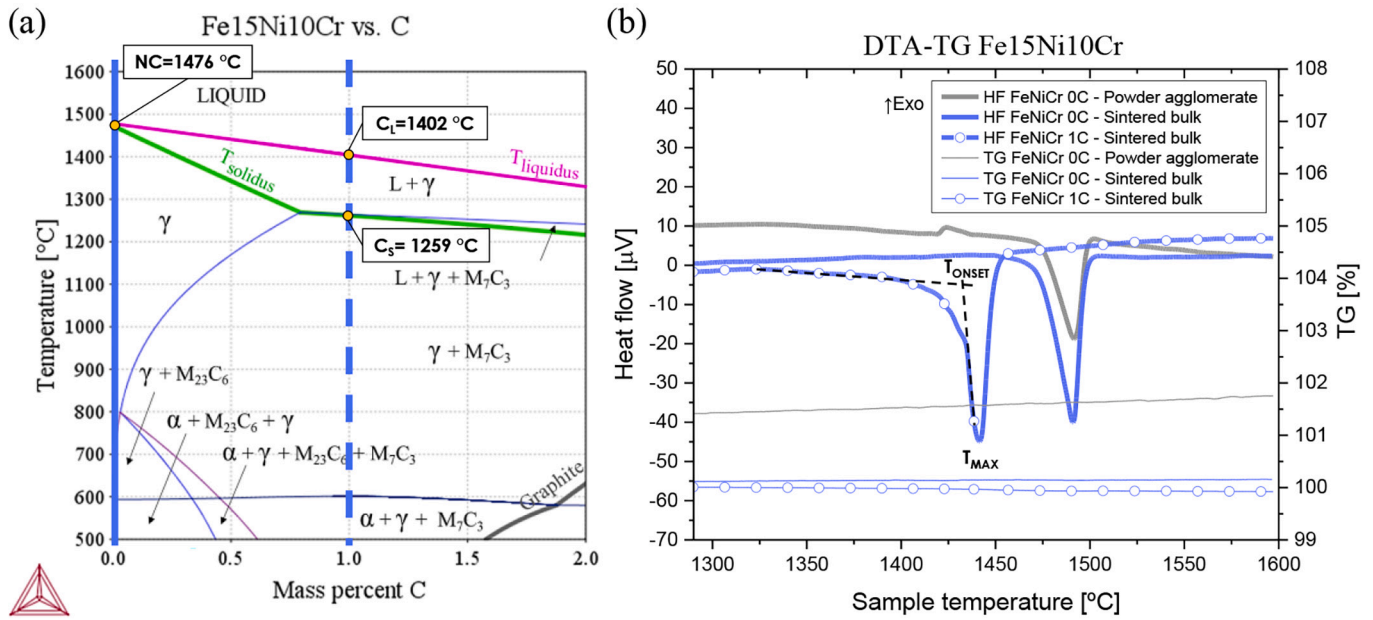


Fig. 8. FESEM images (x5000) in BSE (left) and SE (right) modes of Ti(C,N)-Fe15Cr10Al + 1 wt% C sample processed following a powder metallurgy route (planetary milling + high-vacuum sintering). In the latter, oxide formation is indicated by red circles. (For interpretation of the references to colour in this figure legend, the reader is referred to the web version of this article.)

Table 3

DTA onset and maximum melting temperatures of binder milled powders and sintered bulks. Thermo-Calc® (TC) solidus and liquidus temperatures are also listed, for comparison purposes.

| Composition | Sample type | TC temperatures | | DTA temperatures | |
|--------------------|--------------------|---------------------------|----------------------------|-------------------------|-----------------------|
| | | T _{solidus} [°C] | T _{liquidus} [°C] | T _{ONSET} [°C] | T _{MAX} [°C] |
| Fe15Ni10Cr 0 wt% C | Powder agglomerate | 1476 (NC) | | 1474 | 1492 |
| | Sintered bulk | | | 1470 | 1491 |
| Fe15Ni10Cr-1 wt% C | Sintered bulk | 1259 (C _S) | 1402 (C _L) | 1431 | 1441 |

addition is observed, i.e., substrate region shows mainly the presence of Ti, C and N. Carbides reprecipitated in the metal drop are mostly composed by Ti and C, whereas Fe, Ni and Cr are spotted in the metal region.

Carbide reprecipitation was also observed in the metal drop, with two different morphologies: thick or agglomerated, and thin or needle-like carbides. Their composition, as well as that of the binder in that area, was analysed by EDX. Three measurements per region of interest were done: binder, thick and thin carbides, as displayed in Fig. 12 and Table 4. As it can be appreciated, thick carbides show a metal/carbon ratio similar to M₇C₃ carbide type. Another possibility is that they are essentially Ti(C,N) with a small inclusion of Fe. Last, thin carbides were found to exhibit a typical TiC configuration (with some incorporation of Fe), a composition also observed in the sample with no C for the thicker and more agglomerated carbides [34]. Furthermore, binder element content is virtually the same as for Ti(C,N)-Fe15Ni10Cr system without extra C [34], with a slightly higher C content in the present case (1 wt% C), as expected. It should be noted that both values are believed to be overestimated by the employed technique and parameters, given the analysed metallic area.

Regarding the microstructure of the processed hard material, C addition did not lead to significant variations of either the key parameters – phase amount, carbide diameter or mean free path – or physical and mechanical properties, as evidenced in a previous investigation by the authors of this study [52].

3.1.2. Ti(C,N)-FeCrAl

Aluminium was included in two Fe—Cr systems: Fe15Cr10Al – using elemental powders – and Fe16Cr3Al – employing prealloyed powders.

Ti(C,N)-Fe15Cr10Al (elemental powders). This contact angle experiment was performed using a Ti(C,N) substrate and a Fe15Cr10Al bulk, employing elemental powders and no C addition. This analysis is included in Ref. [34], and a summary of the findings reported there are here included for comparison purposes. As explained in the cited publication and compiled in Table 2, the test was carried out up to 1650 °C, as simulated and DTA (sintered bulk) liquid-formation temperatures were higher for this composition [34]. Nevertheless, the metal sample

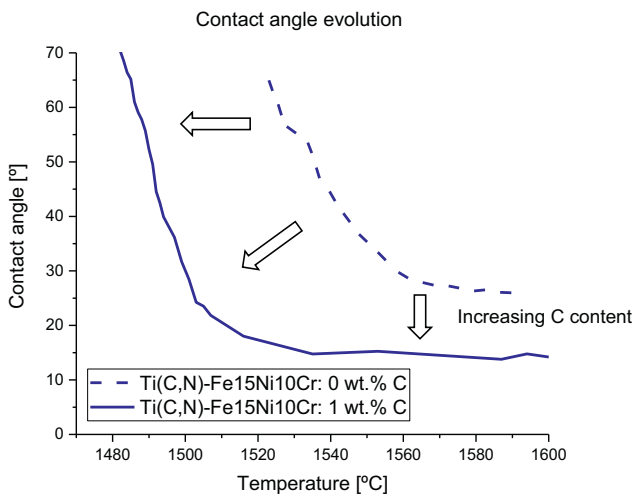


Fig. 9. EDX-mapping of Ti(C,N)-Fe15Cr10Al hard material, showing the elements distribution and confirming oxide formation.

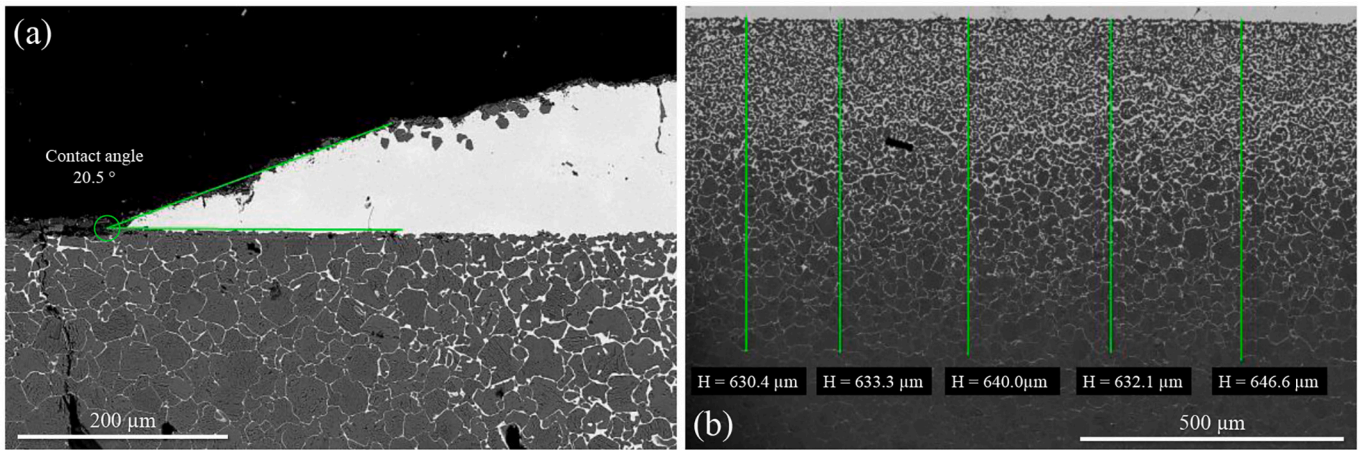


Fig. 10. Ti(C,N)-Fe16Cr3Al hard material phase diagram, using 80 vol% of ceramic phase. Dashed blue line indicates theoretical C content present in the hard material with no C addition. Blue highlighted areas indicate optimum C-windows at 1000 °C. (For interpretation of the references to colour in this figure legend, the reader is referred to the web version of this article.)

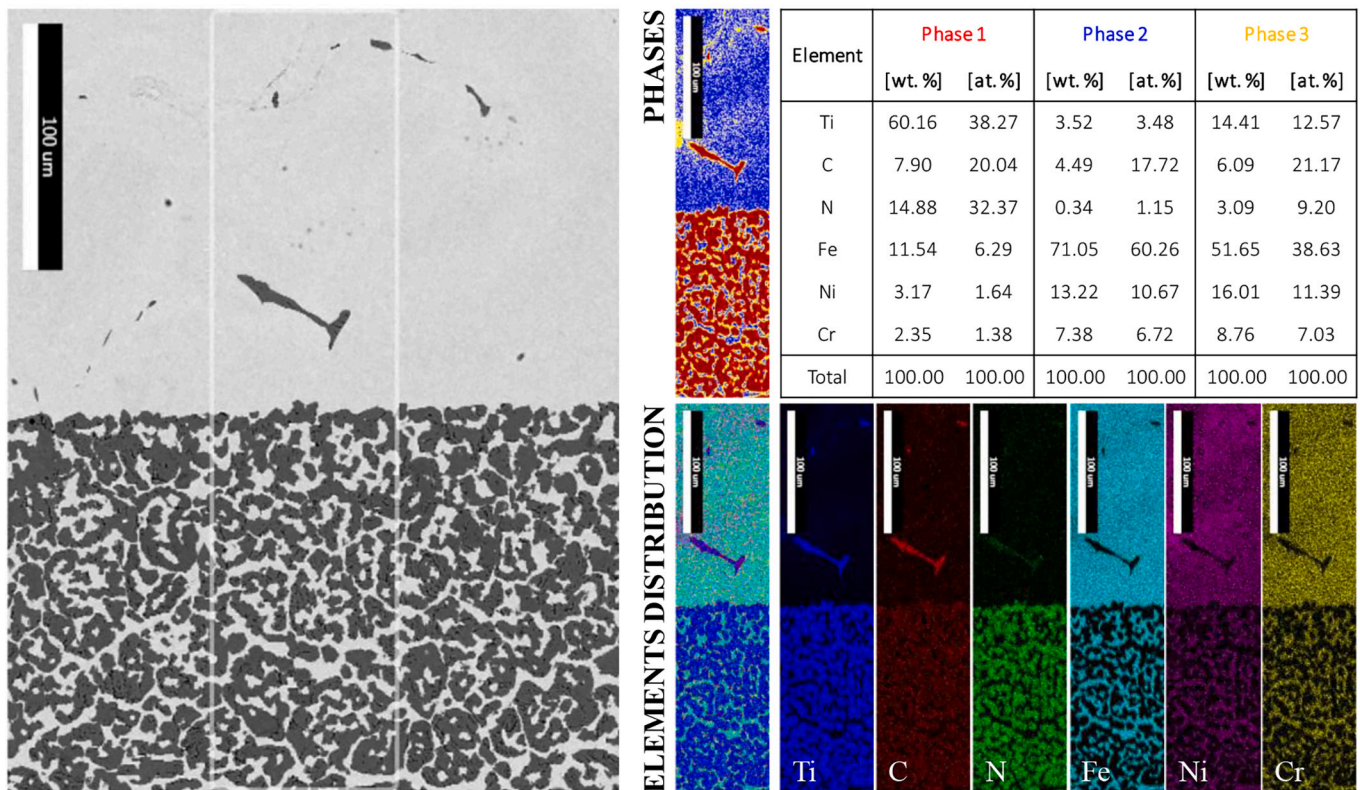


Fig. 11. FESEM-EDX analysis of Ti(C,N)-Fe16Cr3Al (0 wt% C) contact angle. Three zones of interest are indicated in the stitching: (a) carbide reprecipitation, (b) alumina layer at the ceramic-metal limit area, and (c) metal diffusion layer in the ceramic substrate.

did not reach its melting point, probably due to oxidation that this particular alloy composition may experience [16]. There was not any droplet formation; hence, a contact angle could not be measured. Moreover, after cooling there existed no attachment between metallic and ceramic systems; thus, neither transversal cut nor corresponding study could be performed. Nevertheless, a slight trace of interaction from the binder phase could be observed on the substrate surface.

Processing of this composition – following a conventional PM route – led to the microstructure displayed in Fig. 13. It is worth noting that 1 wt % of extra C was added to the material, with the purpose of lowering solidus/liquidus temperatures, avoiding oxidation (by combination of C

and O), and enhancing the sintering behaviour. However, as it can be seen, this composition still led to the formation of large regions of aluminium oxide, yielding poor wettability and porous microstructures, as it could be expected from the wetting experiment. EDX-mapping analysis, collected in Fig. 14, confirmed the nature of inclusions observed in the SE image of Fig. 13, which corresponded to aluminium oxides. Moreover, an uneven distribution of the other alloying elements, i.e., Fe and Cr, was discerned. It should be highlighted that there seems to be a lower volume of binder phase after sintering than for the case where the FeNiCr composition was involved. There are several hypotheses that may explain this phenomenon. One refers to the fact that

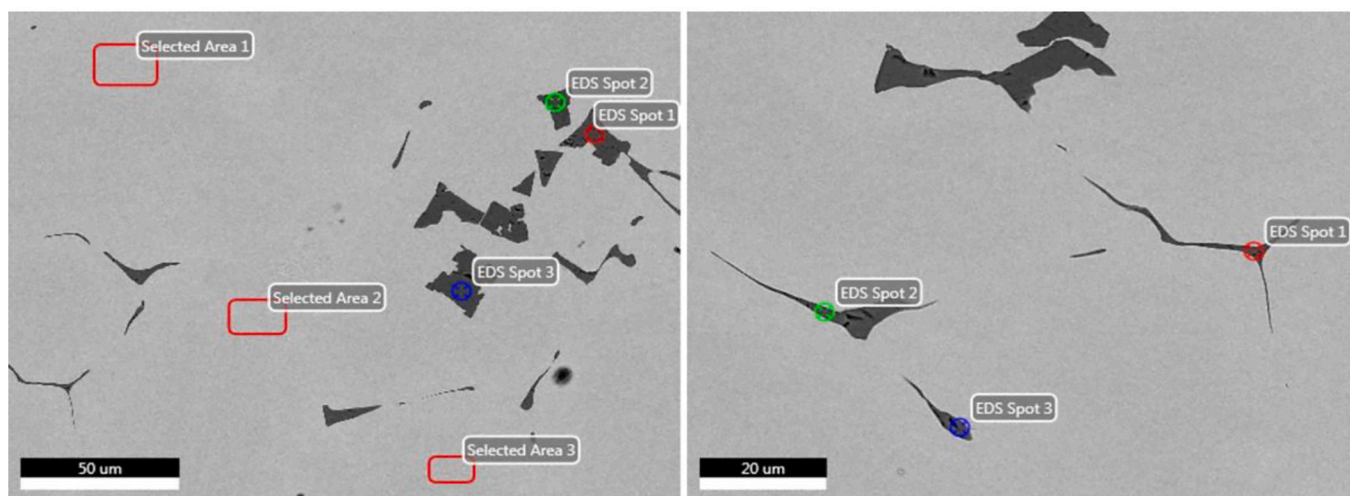


Fig. 12. Mapping analysis of the outermost surface of the metal bulk in Ti(C,N)-Fe16Cr3Al (0 wt% C) contact angle. An aluminium oxide layer formed during the contact angle test between Bakelite (top and black region) and the metal area (bottom and light-grey zone).

Table 4

EDX analysis of the areas and spots indicated in Fig. 12.

| Element | Thick carbide (spots) | Thin carbide (spots) | Binder (areas) |
|-----------|-----------------------|----------------------|----------------|
| Ti | 41.38 ± 0.48 | 42.07 ± 2.48 | 2.85 ± 1.15 |
| C | 35.26 ± 2.90 | 56.61 ± 2.39 | 23.42 ± 0.70 |
| N | 23.05 ± 3.43 | – | – |
| Fe | 0.31 ± 0.28 | 1.31 ± 0.18 | 56.50 ± 2.73 |
| Ni | – | – | 9.74 ± 0.93 |
| Cr | – | – | 7.49 ± 0.07 |
| Total at% | 100 | 100 | 100 |

the binder phase has been dissolved in the ceramic one, aided by the presence of Al. This dissolution of liquid phase (binder) into the solid one (ceramic) would explain the lack of densification during sintering [31]. According to the mapping images (Fig. 14), Al appears to be concentrated in the oxides but also distributed throughout the composite material. A more accurate presence or lack of Al in metal/ceramic phases could be confirmed by Transmission Electron Microscopy (TEM), but such study was out of the scope of the present investigation. Other hypotheses could be related to the sublimation of Al – as its triple point is placed at 933 K [47] – or its migration and concentration at oxide regions, as evidenced in the mapping images of Fig. 14.

Ti(C,N)-Fe16Cr3Al (prealloyed powders). In the light of Fe15Cr10Al results – and with the purpose of reducing the oxygen introduced by

elemental Al powder – a prealloyed powder containing less Al was used - Fe16Cr3Al. Fig. 15 shows the phase diagram of Ti(C,N)-Fe16Cr3Al hard material, employing 80 vol% of ceramic phase. Theoretical C content – without C addition – is indicated by a blue discontinuous line in the diagram. These C values represent the ideal scenario where metallic powders are considered to contain no C, and Ti(C,N) composition coincides with its theoretical setup. As cemented carbide microstructures are considered to ‘freeze’ around 1000 °C [48–50], optimum C-content windows – where graphite precipitation is avoided – are highlighted in blue in this temperature range. It should be noted that, as compared to Fe15Cr10Al binder, the prediction of formation of AlN is somehow more limited. Moreover, this composition also shows lower solidus and liquidus temperatures than for the case corresponding to the Fe15Cr10Al alloy [34].

Wettability of this alloy – using no C addition – on a Ti(C,N) substrate was tested. Table 2 collects the evolution of the bulk morphology as temperature was risen, until reaching a value of 1650 °C. As it can be seen, a drop was not formed. However, the metal sample gradually changed its shape until there was not any gap between its bottom part and the ceramic substrate. After test completion, it could be checked that, although no droplet formed, there existed an attachment between the bulk and the substrate; thus, a transversal cut of the assembly was made to study its cross-section.

Fig. 16 displays a stitching of the transversal section of metal-ceramic assembly resulting from the contact angle test. Three regions of interest are pointed out and analysed:

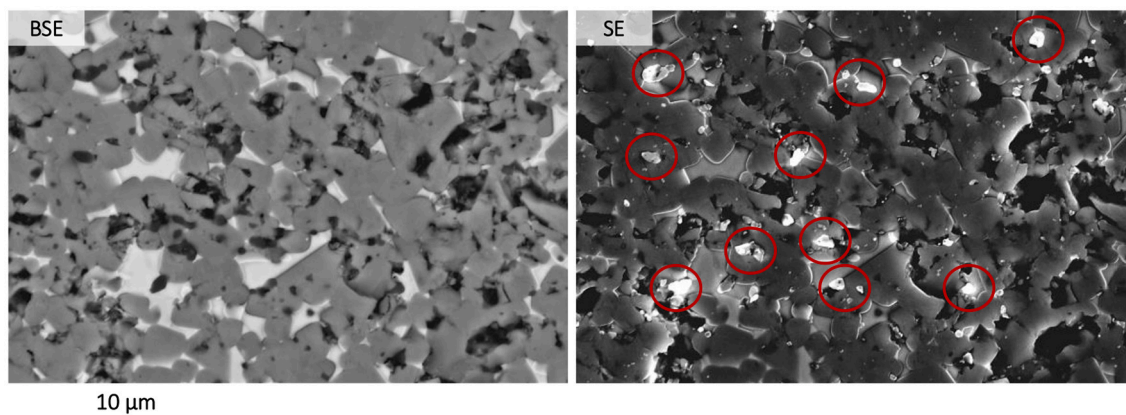


Fig. 13. Microstructure and EDX-mapping of Ti(C,N)-Fe16Cr3Al hard material, processed using a powder metallurgy route (planetary milling + SHIP).

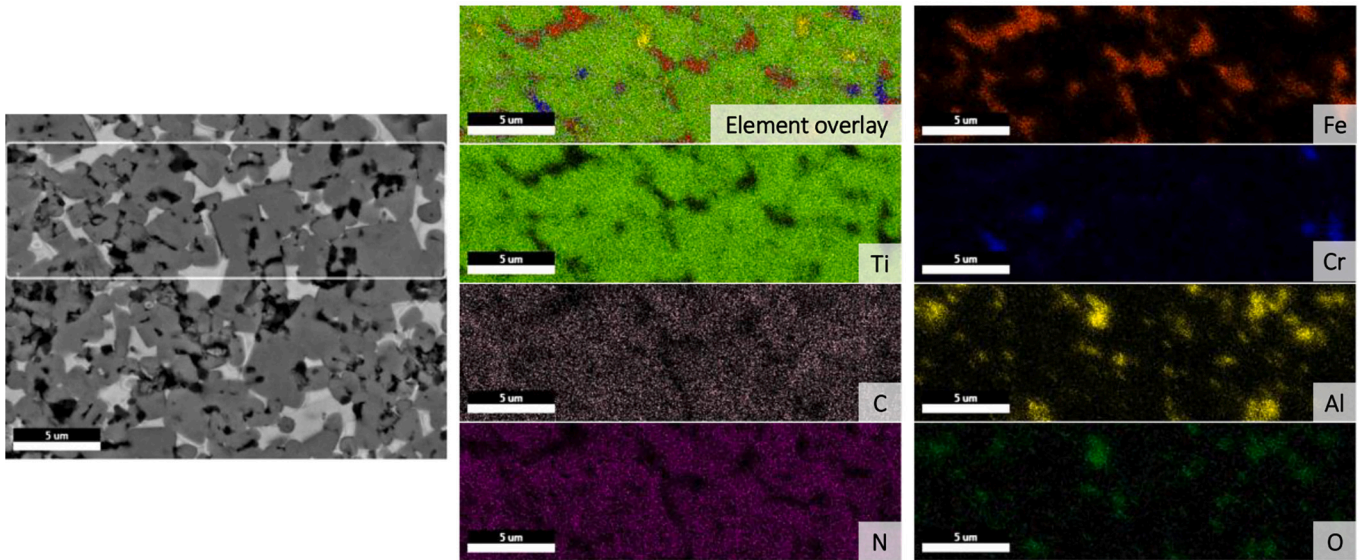


Fig. 14. Correlation between Fe15Ni10Cr solidus/liquidus temperatures, from (a) simulated phase diagrams and (b) DTA-TG analyses, with and without C addition. $T_{solidus}$ and $T_{liquidus}$ are indicated in TC diagrams for compositions without C (NC, No Carbon) and with C (C_S and C_L , respectively). DTA graph shows a detail of T_{ONSET} and T_{MAX} calculation.

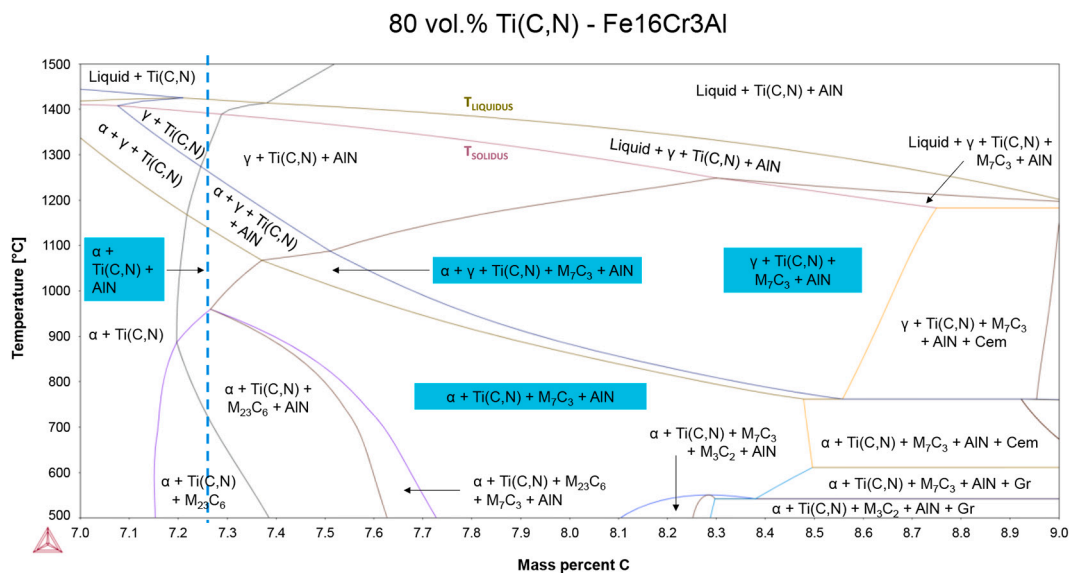


Fig. 15. Comparison of the contact angle evolution of Ti(C,N)-Fe15Ni10Cr system with and without C addition.

Figure 12 (a) Carbide reprecipitation in the metal area. EDX analysis of the carbides showed that there existed two types of Cr-rich carbides: M_3C_2 (Spot 1) and $M_{23}C_6$ (Spots 2 and 3). These carbide configurations were predicted in the hard material phase diagram (Fig. 15). Extra analysis of other carbides also revealed the formation of TiC, as observed in Ti(C,N)-Fe15Ni10Cr system. Moreover, analyses of three different areas were performed in the binder. As it can be appreciated, Al is lost, as only 1 wt% of this element remains in this metal region. This result confirms the microstructural scenario observed for Ti(C,N)-Fe15Cr10Al + 1 wt% C (Fig. 13), i.e., the apparent loss of binder phase and elements after sintering.

Figure 12 (b) At the region where the metal and the ceramic phases meet, a third phase was spotted. EDX analysis and corresponding mappings revealed that it entailed the formation of an aluminium oxide layer, particularly of

Al_2O_3 . This finding allows to speculate about the location of the Al that escaped the metal. Moreover, it would also explain the no-formation of a metal drop, as a layer of this oxide was also observed to be surrounding the exterior part of the bulk – as confirmed by EDX analysis and corresponding mapping (Fig. 17) – hindering a complete liquidus and droplet formation. This phenomenon also demonstrates and confirms the reason for the absence of any droplet in all the other contact angle tests of this project where the binder contained Al, i.e., the high affinity between this element and oxygen. In accordance with the hypothesis of the formation of Al oxides, the removal of Al from the metal binder is confirmed, as enlightened also in the mappings of Fig. 14.

Figure 12 (c) Last region consists of the metal penetration or diffusion layer into the substrate, responsible for the attachment of the bulk to the substrate. It points out a good interaction

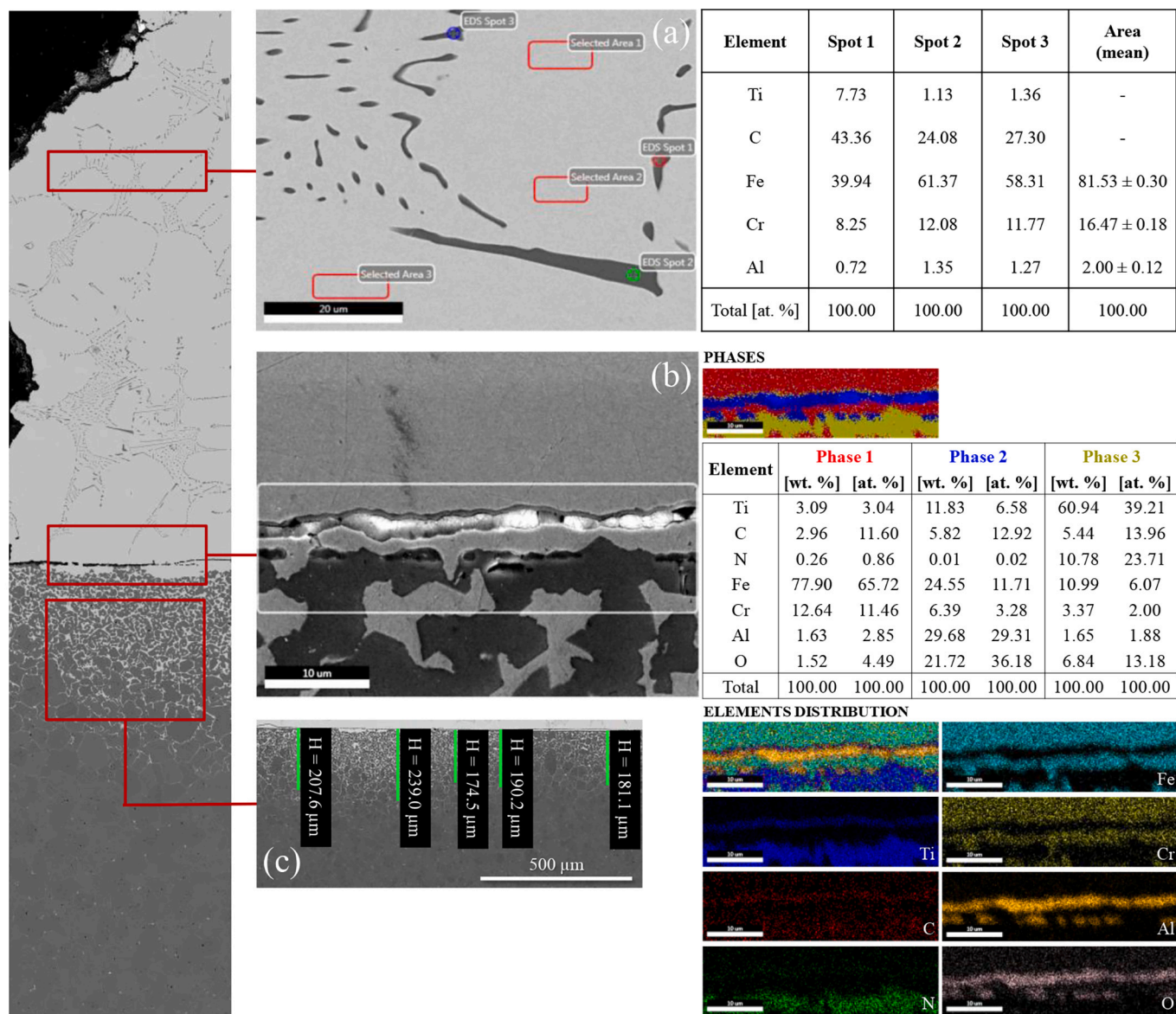


Fig. 16. FESEM images of Ti(C,N)-Fe15Ni10Cr (1 wt% C) contact angle cross-section, with measurements of (a) droplet-substrate angle and (b) metal penetration layer.

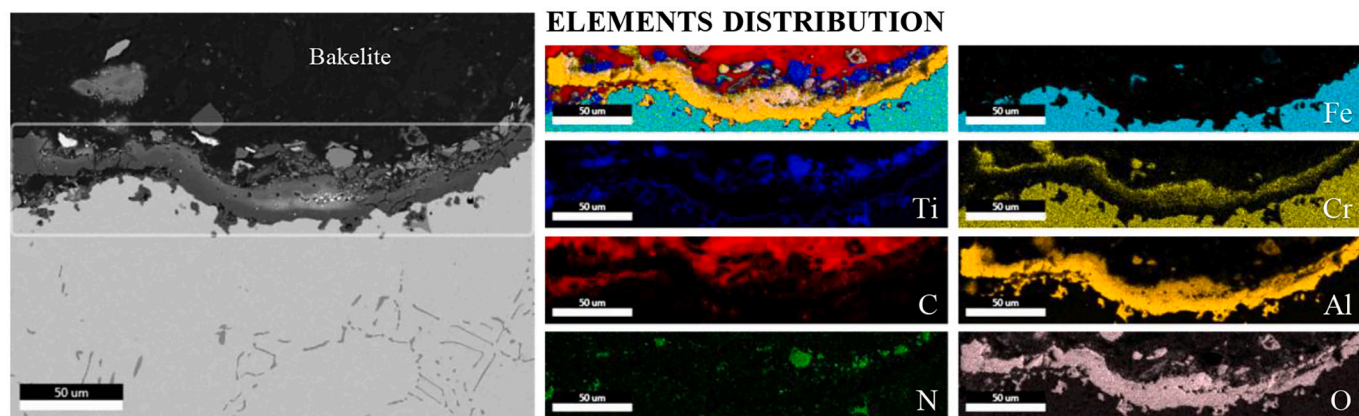


Fig. 17. Mapping analysis (15 kV) of Ti(C,N)-Fe15Ni10Cr (1 wt% C) metal/ceramic region showing the present phases and elements distribution.

between FeCrAl and Ti(C,N). A mean depth of $198 \pm 27 \mu\text{m}$ was determined. It is believed that the formation of the alumina layer impeded diffusion; and thus, to get a thicker binder layer.

Processing of the hard material led to the heterogeneous microstructure observed in Fig. 18. As it can be appreciated, aluminium-oxide formations – as confirmed by EDX-mapping analyses – surrounded binder pools. Porosity could also be spotted and measured. It should be noted that extra C was also used in this processed sample. The large binder areas point out a compromised metal-ceramic wettability. These findings are in consonance with the ones observed in the wetting test and showed the improvement in metal-ceramic interaction with respect to the elemental composition (Fe15Cr10Al). The prealloyed system revealed that, although no droplet effectively formed, higher fusion resulted in the attachment of the metal bulk to the ceramic substrate. This translated into an improved sintering behaviour, as compared to that resulting for the system involving Fe15Cr10Al, but eventually it could not achieve a competitive metal-ceramic microstructure.

3.2. Wettability on WC

Contact-angle tests were also performed on WC substrates with the purpose of comparing the wettability scenario with respect to Ti(C,N) ones. In doing so, Fe15Ni10Cr, Fe15Cr10Al and Fe16Cr3Al alloys, without C addition, were studied. Thus, as performed with Ti(C,N), this section will be divided into the two types of alloys employed: FeNiCr and FeCrAl.

3.2.1. WC-FeNiCr

Wettability of Fe15Ni10Cr binder, with no addition of C, was evaluated on a WC substrate. Contact angle evolution for this assembly, collected in Table 2, shows the formation of the liquidus phase and its evolution for this composition, which took place around 1400°C . Hence, heating was stopped at 1500°C , to keep a similar temperature range of approximately 100°C between the drop formation and final temperature, as performed with systems involving Ti(C,N) as the ceramic phase. In this case, an effective droplet was not formed. Instead, the metallic bulk in contact with the ceramic substrate – i.e., at the metal-ceramic interface – gradually melted, spreading over the ceramic surface and infiltrating into the substrate. Very interesting, previous studies revealed a different wetting dynamic of Co [41] and Cu [42] as binder phases on WC-based substrates, where a droplet between the molten metal and the ceramic was observed and a contact angle value could be effectively measured. With respect to carbide comparison, it is also worth noting

this dissimilar behaviour with respect to Ti(C,N) substrate in the present study, which is believed to be related to the different transition of the binder to liquidus state, as shown in the phase diagrams of the composites [34]. As it can be seen, at 0 wt% of extra C addition this binder evolution is gradual in the case of Ti(C,N)-Fe15Ni10Cr, attaining the mixed $L + \gamma$ region before completely transforming into liquid. Contrarily, for WC-Fe15Ni10Cr composition, there is a direct transformation $\gamma \rightarrow L$ at 1243°C for this C content. At the surface, no effective measurement of a contact angle could be performed; thus, it could be estimated to be 0° , giving sign of very good metal-ceramic wettability. Moreover, the dissimilar wetting behaviour of FeNiCr on Ti(C,N) and WC can be also explained by the developed surface energies among the binder, the ceramic phase and their boundary region, as explained by Gren and Wahnström [53]. They relate the spreading parameter (S) of the liquid metallic phase (M) on the solid ceramic substrate (WC, in their study) to the difference of dry and wet interfacial energies. This is described in Eq. (2), where σ_{WC} stands for the surface energy of WC, $\gamma_{WC/M}$ for WC/M phase-boundary energy, and σ_M for the binder surface energy:

$$S = \sigma_{WC} - (\gamma_{WC/M} + \sigma_M) \quad (2)$$

If $S > 0$, indicating that the interface energy is larger in the dry case, there is perfect wetting. In the present investigation, this scenario would correspond to what observed in WC-FeNiCr assembly, thus confirming that positive wetting behaviour. On the other hand, if $S < 0$, there is only partial wetting, described by the contact angle θ and Young's equation (Eq. (1)), the scenario observed for Ti(C,N) in the present investigation.

After cooling, the sample was cut transversally to study its cross section by FESEM and EDX. For the analysis of this sample, CBS detector in 'A+B-C-D' mode was used, as explained in the *Experimental procedure* section. The high magnification needed to correctly spot the metal binder complicated the measurement of the metallic diffusion layer. It could be finally estimated by performing a stitching of FESEM images of the whole transversal section. FeNiCr was found to diffuse up to 2 mm from the top ceramic surface, giving sign of excellent metallic-ceramic interaction by dissolution and diffusion phenomena. It is also worth noting the irregularity of the top surface of the contact angle. Fig. 19 shows FESEM images of the cited region at two different magnifications. Image (a) corresponds to the lower magnification one, i.e., x250. Due to the CBS mode employed – 'A+B-C-D' –, the mounting resin (Bakelite) used to embed the sample is shown in white colour. On the other hand, ceramic and metallic phases can be appreciated in different grey nuances. Image (b) shows a higher magnification of this area, i.e., x2000. A yellow rectangle surrounds the metal-ceramic region that will be

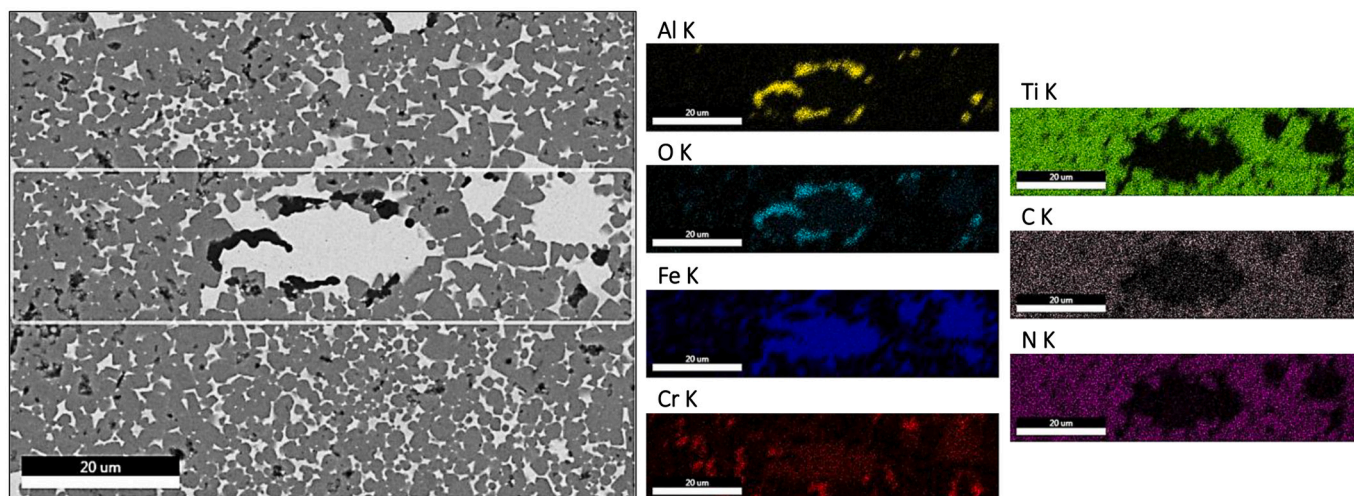


Fig. 18. FESEM images indicating the analysed areas and spots in the metal drop of Ti(C,N)-Fe15Ni10Cr (1 wt% C) contact angle.

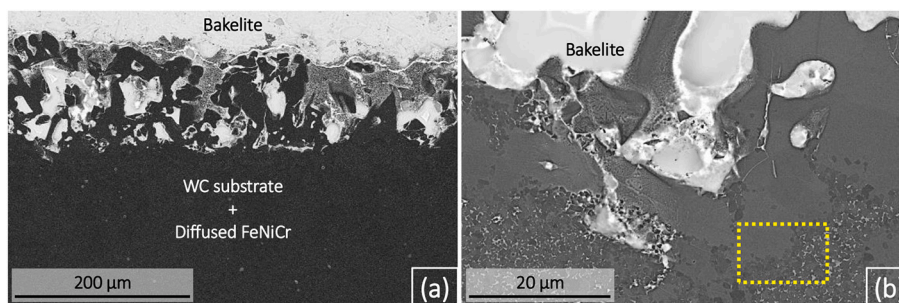


Fig. 19. FESEM images (CBS, 'A+B-C-D' mode) of the top surface of WC-Fe15Ni10Cr (0 wt% C) contact angle. Two different magnifications are shown: (a) x250 and (b) x2000. Bakelite and hard material phases are indicated. In the latter, the type of area analysed hereinafter is pointed out by a yellow rectangle. (For interpretation of the references to colour in this figure legend, the reader is referred to the web version of this article.)

characterised hereinafter by mapping and EDX analyses.

Fig. 20 displays a FESEM image and mapping analysis of the type of area highlighted in Fig. 19, which has been rotated 90°. As it can be observed, two phases were spotted, corresponding essentially to WC and FeNiCr binder. Nevertheless, as the FESEM image reveals, three distinct phases with different contrasts were discerned. They were separately analysed by EDX, labelling each zone as A (binder), B (WC particles) and C (a transition-like region). Composition in at% of these zones is listed in Table 5. The third phase, C, is believed to correspond to eta-phase (η -phase), as a previous publication addressing a WC-FeNiCr composition has reported a similar C content for this phase [54]. An additional experimental fact supporting the ceramic nature of this phase is its contrast when all the detectors of the FESEM are activated. Fig. 21 shows the same analysed region but using 'All' mode of the CBS detector. As it can be appreciated, phase C is also visible and shows a similar – although slightly darker – contrast to WC particles (B). Interestingly, this experimental result differs from Thermo-Calc® prediction for M_6C composition in WC-Fe15Ni10Cr hard material, as Table 6 shows. Nevertheless, this discrepancy may lie on the fact that a fixed composition is used in the prediction whereas, in the case of the contact angle test, carbide/binder ratio varies depending on the observed or analysed region. Another hypothesis entails the overestimation of the C content measured

Table 5

EDX analysis (at%) of A, B and C zones labelled in Fig. 20.

| Element | A | B | C |
|-------------|--------------|--------------|--------------|
| W | 12.66 ± 1.88 | 19.05 ± 2.16 | 15.36 ± 1.77 |
| C | 49.74 ± 8.72 | 80.41 ± 2.81 | 60.39 ± 5.29 |
| Fe | 27.86 ± 5.38 | 0.54 ± 0.94 | 17.86 ± 2.34 |
| Ni | 7.43 ± 1.30 | – | 3.02 ± 0.37 |
| Cr | 2.31 ± 0.28 | – | 3.37 ± 0.90 |
| Total [at%] | 100.00 | 100.00 | 100.00 |

by EDX (Table 5), especially noticeable in the analysis of the binder (point A) and WC phase (point B), where 50 and 80 at% of C were obtained, respectively. This was also observed in the C content of the binder area in Table 4.

Fig. 22 collects FESEM-CBS images – in 'All' and 'A+B-C-D' modes, respectively – of the microstructure of a WC-Fe15Ni10Cr, after processing by PM. As it can be seen, they display homogeneous microstructures and an excellent dispersion of the carbides in the binder phase. Differences can be noted between the final sintered structures for Ti(C,N)-Fe15Ni10Cr (Fig. 7) and this WC-based sample, in agreement with the dissimilar wetting scenarios observed in the contact angle test

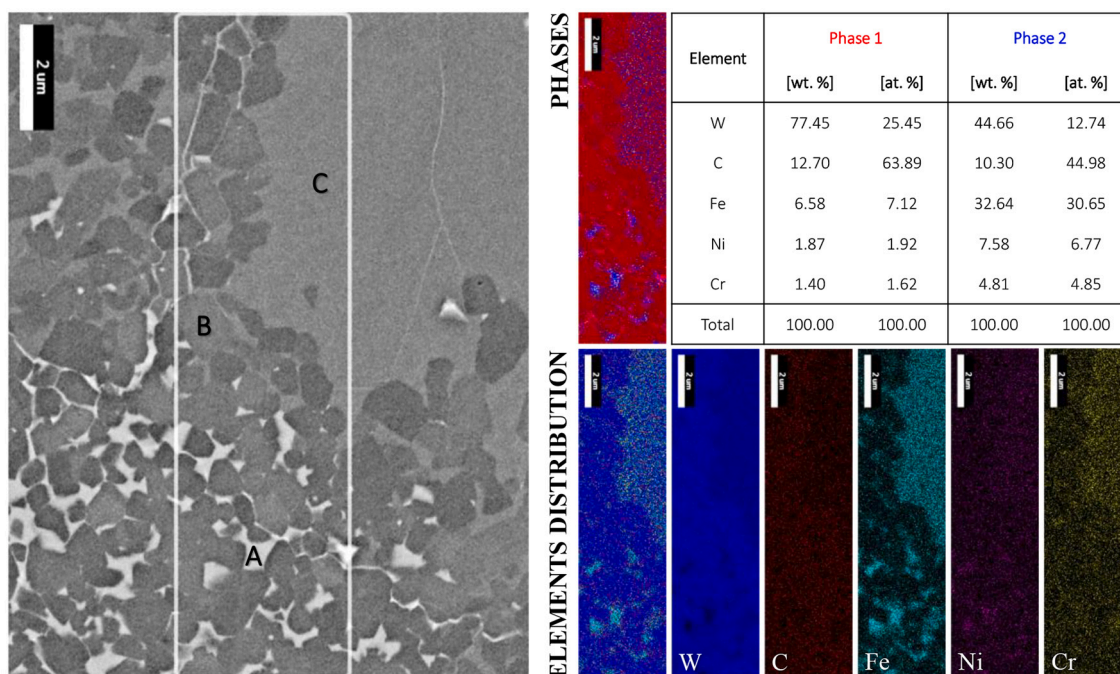


Fig. 20. FESEM image (CBS, 'A+B-C-D' mode) of the contact angle region analysed by EDX, showing the three zones of interest – A, B and C –, and mapping analysis of WC-Fe15Ni10Cr (0 wt% C) metal/ceramic region displaying the phases present as well as element distribution.

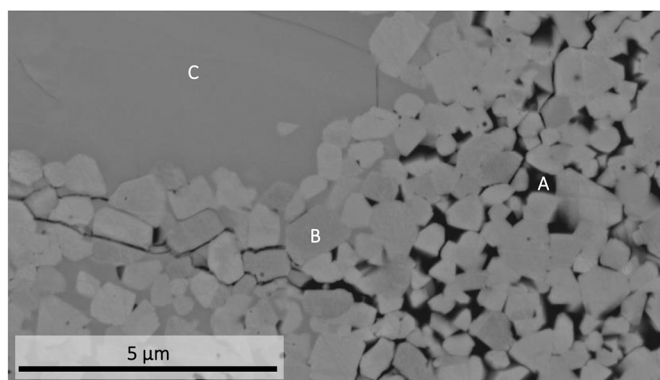


Fig. 21. FESEM image (CBS, 'All' mode) showing the same analysed region of WC-Fe15Ni10Cr (0 wt% C) contact angle but activating all the layers of the FESEM detector.

Table 6

Thermo-Calc® predicted molar fraction for M_6C compound in WC-Fe15Ni10Cr hard material with 0 wt% C addition (5.44 wt% C) at 1000 °C.

| Element | M_6C |
|---------|--------|
| W | 36.22 |
| C | 14.29 |
| Fe | 40.97 |
| Ni | 4.23 |
| Cr | 4.29 |
| Total | 100.00 |

results. On the one hand, contact angle experiments on systems involving Ti(C,N) substrates showed a proper wettability scenario – with an angle value of 26° – and clear metal-ceramic interaction, where solution-reprecipitation phenomena could be evidenced. On the other hand, wettability tests made on systems using WC substrates yielded an even lower angle value – 0° –, where dissolution of smaller carbide particles could also be appreciated. Thus, even though the same amount and mean particle size of ceramic phase was introduced in the powder mixtures, the dissimilar wettability, dissolutive behaviour and metal-ceramic interaction during LPS experienced by these distinct hard phases explain the final different features observed.

3.2.2. WC-FeCrAl

As conducted with Ti(C,N) phase, two FeCrAl compositions were tested on WC: Fe15Cr10Al – using elemental powders – and Fe16Cr3Al –

employing prealloyed ones.

WC-Fe15Cr10Al (elemental powders). For Fe15Cr10Al alloy, using no C addition and tested on a WC substrate, final heating temperature was 1650 °C. As displayed in Table 2, although intensive heating was imposed, no droplet formed. There were slight changes in the morphology of the bulk, especially noticeable in the bottom part of the metal bulk. However, there was no trace of liquid phase formation or wetting on the ceramic substrate. Hence, the same results were attained by this alloy, independent of the hard phase employed. There was not any attachment of the bulk to the ceramic substrate.

In the light of the oxidation that occurred in the Ti(C,N)-Fe15Cr10Al sample (Fig. 13 and Fig. 14), WC-Fe15Cr10Al samples were not processed. Instead, the prealloyed powder – Fe16Cr3Al – was directly used for the study of the WC-FeCrAl system.

WC-Fe16Cr3Al (prealloyed powders). Following the above ideas, the prealloy composition was tested on a WC substrate, adding no extra C, as it has been previously performed with Ti(C,N) substrate. WC-Fe16Cr3Al phase diagram is displayed in Fig. 23. As observed for the Ti(C,N)-based composition, Fe16Cr3Al shows lower solidus and liquidus temperatures than the hard materials combined with the Fe15Cr10Al alloy [34].

The high-temperature experiment was also carried out until reaching 1650 °C. Adapted camera pictures of this metal-ceramic assembly can be retrieved in Table 2. At 185 °C, the initial morphology of the system may be seen. When a temperature of 551 °C is attained, slight fusion can be appreciated in the left part of the bulk-substrate contact line, indicated by a light-blue arrow in the image. No significant changes are spotted until 1508 °C, where massive melting at the base of the metal specimen can be evidenced, also highlighted by light-blue arrows, as the third image displays. Finally, at 1650 °C, some formations can be recognised. They seem to be linked to oxidation of the liquid phase that previously formed.

The findings discerned after test completion evidenced that no metal bulk was adhered to the ceramic substrate and a crater was spotted where it was placed, coinciding with the formations observed in the contact angle camera. There was trace of binder interaction or wettability on the surface of the ceramic substrate, more evidently than in the cases where Fe15Cr10Al alloy and Ti(C,N)-Fe16Cr3Al system were involved. Such experimental fact indicates a better wetting behaviour of the prealloy with respect to the elemental composition, as expected from the earlier fusion observed in the images from the adapted camera. Nevertheless, oxide formation also took place, as evidenced in the bulk of Ti(C,N)-Fe16Cr3Al sample, and in a more abrupt manner, as indicated by the crater formation. Neither droplet nor attachment of the metal occurred; hence, no characterisation of the cross-section could be performed.

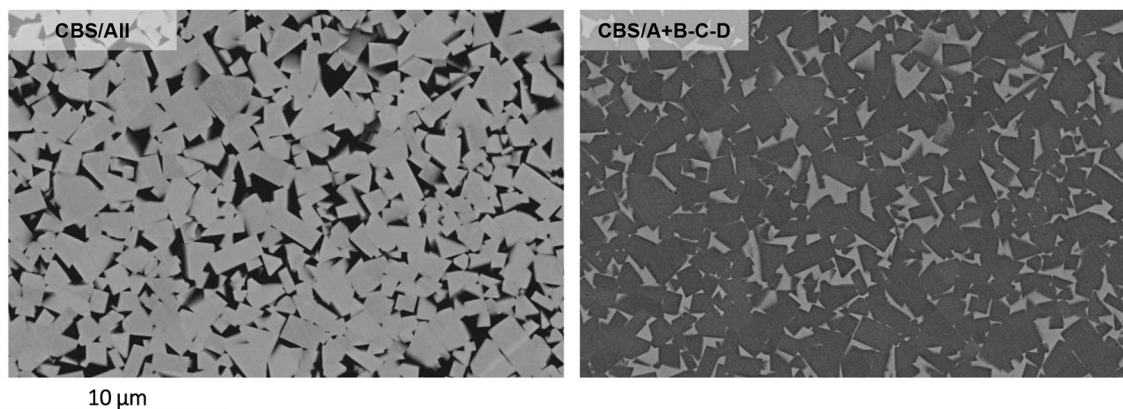


Fig. 22. FESEM micrographs (x5000) of WC-Fe15Ni10Cr samples, processed following a PM route (attritor milling + SHIP). Images in both CBS modes, 'All' (left) and 'A+B-C-D' (right), are shown.

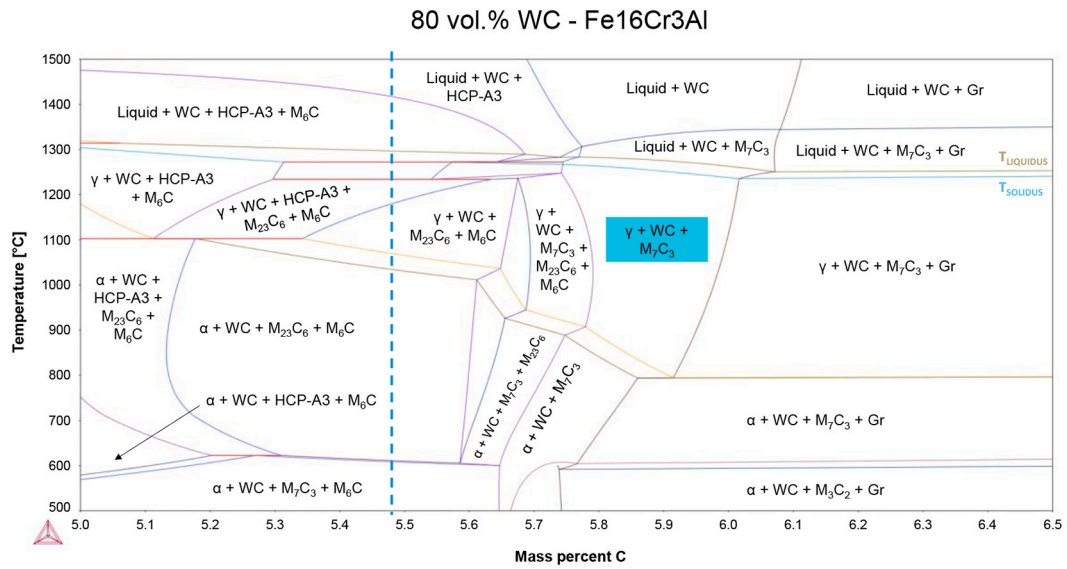


Fig. 23. WC-Fe16Cr3Al hard material phase diagram, using 80 vol% of ceramic phase. Dashed blue line indicates theoretical C content present in the hard material with no C addition. Blue highlighted area indicates optimum C-window at 1000 °C. (For interpretation of the references to colour in this figure legend, the reader is referred to the web version of this article.)

Fig. 24 gathers information on microstructure and EDX-mapping analysis of the WC-Fe16Cr3Al processed sample. A heterogeneous scenario is clearly depicted. As for the Ti(C,N)-Fe16Cr3Al system, black inclusions of aluminium oxide could be spotted, either within or surrounding binder pools. Nevertheless, these binder areas appear to be smaller and more dispersed than for the Ti(C,N)-based sample, pointing out a slightly improved wettability of FeNiCr on WC. This is in agreement with the more pronounced metallic diffusion on the surface of WC substrate, as compared to the Ti(C,N) one in contact angle tests. It should be noticed that different C contents were studied, but neither full density nor a homogeneous microstructure was achieved with none of them.

4. Conclusions

In this investigation, high-temperature wettability of different configurations of hard materials – employing Fe-based binders, and Ti(C,N) or WC as ceramic phase – were analysed. These contact angle tests belong to the validation step of a methodology proposed by the authors in a previous contribution [34] for the design and production of

alternative hard materials. Wetting experiments were conducted and corresponding results were presented using either binder or ceramic phases as experimental variable. On the one hand, tests involving FeNiCr/FeCrAl alloys – employing Ti(C,N) as hard phase – were contrasted. Here, the effect of C addition on wettability was also assessed. On the other hand, tests on WC- FeNiCr/FeCrAl samples were carried out, and experimental findings were compared to those previously reported in Ti(C,N) samples. As a proof of concept, contact angle results were linked to the final microstructures obtained after processing the samples by PM. The following conclusions could be drawn:

Binder comparison

- Fe15Ni10Cr binder evidenced a satisfactory wetting behaviour on Ti (C,N), achieving a low contact angle accompanied by dissolution of Ti(C,N) particles, penetration of the binder into the ceramic substrate, and carbide reprecipitation at the metal drop region.

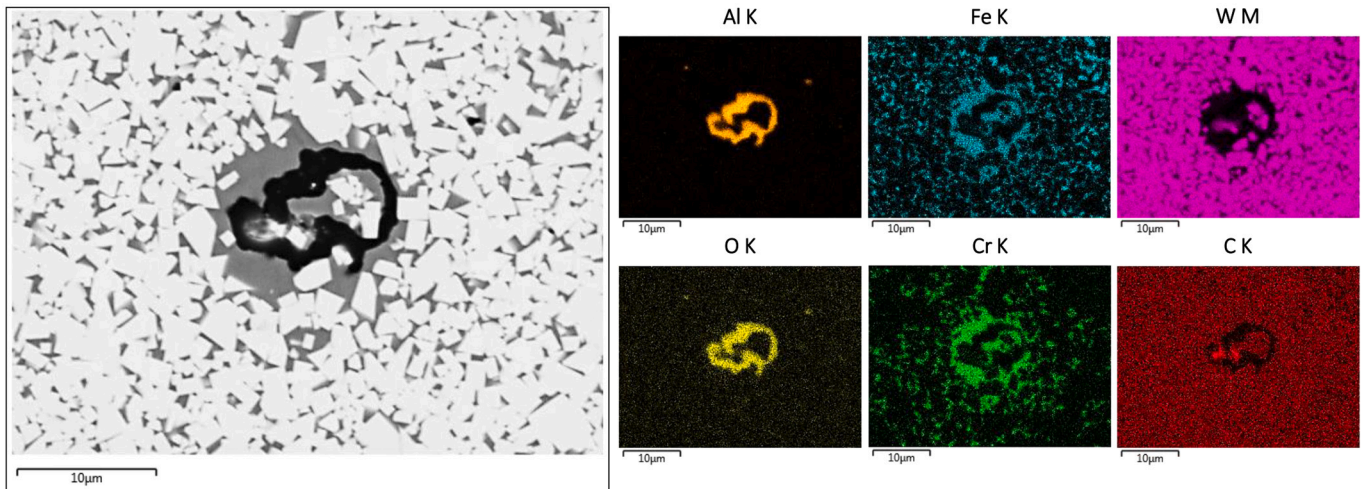


Fig. 24. Microstructure and EDX-mapping of WC-Fe16Cr3Al hard material, processed using a powder metallurgy route (planetary milling + SHIP).

- C addition led to an improvement of the wettability scenario, with a reduction in the contact angle value and an extension of the metal diffusion layer into the ceramic substrate.
- Fe15Cr10Al phase gave sign of oxidation that hindered an accurate wettability assessment. Neither droplet nor adhesion between the metal bulk and either substrate took place. The metal experienced some fusion or morphology change, leaving a slight trace of its presence on the ceramic substrate. However, no further effects were discerned.
- With the purpose of avoiding oxidation, a prealloy powder with composition Fe16Cr3Al was employed. Assessment of its wetting behaviour on a Ti(C,N) substrate revealed that, although no droplet effectively formed, higher fusion resulted in the attachment of the metal bulk to the ceramic substrate. Evaluation of its transversal cut allowed to identify a layer of Al oxide surrounding the metal bulk, confirming the inability to form a droplet due to oxidation. Carbide reprecipitation in the metal region and binder diffusion into the substrate were observed, indicating a good ceramic-metallic interaction shaded by the affinity of aluminium to oxygen.

Carbide comparison

- Testing of FeNiCr binder with WC substrate resulted in complete melting and spreading of the metal on the ceramic surface, estimating a final 0° contact angle.
- As with Ti(C,N), in WC-Fe15Cr10Al sample, oxidation hindered a correct assessment of wettability and attachment of the metallic bulk to the ceramic substrate.
- In the case of WC-Fe16Cr3Al system, neither droplet nor attachment of the metal occurred. Nevertheless, there was more evident trace of binder interaction or wettability on the surface of the ceramic substrate than with Ti(C,N). This suggested a better wetting behaviour with WC phase.

Microstructural inspection of the samples after processing by PM revealed excellent consonance between contact angle and sintering scenarios. Thus, the effectiveness of contact angle testing for the prediction and modelling of hard material sinterability is validated in this study.

CRedit authorship contribution statement

M. de Nicolás-Morillas: Conceptualization, Data curation, Formal analysis, Funding acquisition, Investigation, Methodology, Project administration, Software, Validation, Visualization, Writing – original draft, Writing – review & editing. **L. Llanes:** Conceptualization, Formal analysis, Funding acquisition, Investigation, Methodology, Project administration, Resources, Supervision, Validation, Writing – review & editing. **E. Gordo:** Conceptualization, Formal analysis, Funding acquisition, Investigation, Methodology, Project administration, Resources, Supervision, Validation, Writing – review & editing.

Declaration of Competing Interest

The authors declare that they have no known competing financial interests or personal relationships that could have appeared to influence the work reported in this paper.

Data availability

The data that has been used is confidential.

Acknowledgements

The current investigation was supported by the Spanish Government (*Agencia Estatal de Investigación*) and European Union through the

project AEI/10.13039/501100011033 (PID2019-106631GB-C41/C43) and grants BES-2016-077340 and *Margarita Salas*, as well as the Regional Government of Madrid through the program ADITIMAT, ref. S2018/NMT-4411. The authors would like to acknowledge and thank CERATIZIT Group (Mamer, Luxembourg), for their contribution to the processing of the hard materials, and Johannes Pötschke, from Fraunhofer Institute for Ceramic Technologies and Systems IKTS, for providing binderless WC substrates. Funding for APC: Universidad Carlos III de Madrid (Read & Publish Agreement CRUE-CSIC 2022).

References

- [1] *Comprehensive Hard materials – volume I: Hardmetals. Section I: introduction to Hardmetals*, in: V.K. Sarin, D. Mari, L. Llanes, C.E. Nebel (Eds.), *Compr. Hard Mater*, Elsevier, Oxford (UK), 2014, pp. 1–120.
- [2] European Commission, Communication from the Commission to the European Parliament, the Council, the European Economic and Social Committee and the Committee of the Regions — *Critical Raw Materials Resilience: Charting a Path towards Greater Security and Sustainability*, COM(2020) 474, Brussels (Belgium), 2020.
- [3] European Commission, REACH REFIT Evaluation (REACH Review). https://ec.europa.eu/growth/sectors/chemicals/reach/review_en, 2017 accessed January 10, 2021.
- [4] Report on Carcinogens, Fourteenth edition, US Natl. Toxicol. Progr., 2016. <https://ntp.niehs.nih.gov/>. accessed February 13, 2021.
- [5] US National Toxicology Program (NTP). <https://ntp.niehs.nih.gov/>, 2021.
- [6] G.S. Upadhyaya, *Cemented Tungsten Carbides: Production, Properties and Testing*, Noyes Publications, New Jersey (US), 1998.
- [7] E. Gordo, L. Prakash, Editorial for Special Section on “New approaches for novel cermets”, *Int. J. Refract. Met. Hard Mater.* 63 (2017) 1, <https://doi.org/10.1016/j.ijrmhm.2016.12.005>.
- [8] J. García, V. Collado Ciprés, A. Blomqvist, B. Kaplan, Cemented carbide microstructures: a review, *Int. J. Refract. Met. Hard Mater.* 80 (2019) 40–68, <https://doi.org/10.1016/j.ijrmhm.2018.12.004>.
- [9] Commodity Prices, *Trading Econ.* <https://tradingeconomics.com/commodities>, 2021 accessed December 14, 2021.
- [10] K. Aigner, W. Lengauer, P. Eitmayr, Interactions in iron-based cermet systems, *J. Alloys Compd.* 262–263 (1997) 486–491, [https://doi.org/10.1016/S0925-8388\(97\)00360-5](https://doi.org/10.1016/S0925-8388(97)00360-5).
- [11] J.A. Canteli, J.L. Cantero, N.C. Marín, B. Gómez, E. Gordo, M.H. Miguélez, Cutting performance of TiCN–HSS cermet in dry machining, *J. Mater. Process. Technol.* 210 (2010) 122–128, <https://doi.org/10.1016/j.jmatprotec.2009.08.003>.
- [12] S. Norgren, J. García, A. Blomqvist, L. Yin, Trends in the P/M hard metal industry, *Int. J. Refract. Met. Hard Mater.* 48 (2015) 31–45, <https://doi.org/10.1016/j.ijrmhm.2014.07.007>.
- [13] G. Gille, J. Bredthauer, B. Gries, B. Mende, W. Heinrich, Advanced and new grades of WC and binder powder – their properties and application, *Int. J. Refract. Met. Hard Mater.* 18 (2000) 87–102, [https://doi.org/10.1016/S0263-4368\(00\)00002-0](https://doi.org/10.1016/S0263-4368(00)00002-0).
- [14] R. Subramanian, J.H. Schneibel, FeAl–TiC and FeAl–WC composites—melt infiltration processing, microstructure and mechanical properties, *Mater. Sci. Eng. A* 244 (1998) 103–112, [https://doi.org/10.1016/S0921-5093\(97\)00833-2](https://doi.org/10.1016/S0921-5093(97)00833-2).
- [15] C.M. Fernandes, A.M.R. Senos, Cemented carbide phase diagrams: a review, *Int. J. Refract. Met. Hard Mater.* 29 (2011) 405–418, <https://doi.org/10.1016/j.ijrmhm.2011.02.004>.
- [16] R. Furushima, K. Katou, K. Shimojima, H. Hosokawa, M. Mikami, A. Matsumoto, Effect of η -phase and FeAl composition on the mechanical properties of WC–FeAl composites, *Intermetallics*. 66 (2015) 120–126, <https://doi.org/10.1016/j.intermet.2015.06.023>.
- [17] M.S. Archana, V.V.S.S. Srikanth, S.V. Joshi, J. Joardar, Influence of applied pressure during field-assisted sintering of Ti(C,N)–WC–FeAl based nanocomposite, *Ceram. Int.* 41 (2015) 1986–1993, <https://doi.org/10.1016/j.ceramint.2014.09.022>.
- [18] R.F. Santos, A.M.F. Rocha, A.C. Bastos, J.P. Cardoso, F. Rodrigues, C.M. Fernandes, J. Sacramento, M.G.S. Ferreira, A.M.R. Senos, C. Fonseca, M.F. Vieira, L. F. Malheiros, The effect of Cr content on the corrosion resistance of WC–Ni–Cr–Mo composites, *Int. J. Refract. Met. Hard Mater.* 95 (2020), 105434, <https://doi.org/10.1016/j.ijrmhm.2020.105434>.
- [19] B. Bozzini, A. Gianoncelli, G. Kourousias, M. Boniardi, A. Casaroli, S. Dal Zilio, R. Hussain, M.K. Abyaneh, M. Kiskinova, C. Mele, S. Tedeschi, G. Pietro De Gaudenzi, The role of chromium in the corrosion performance of cobalt- and cobalt-nickel based hardmetal binders: a study centred on X-ray absorption microspectroscopy, *Int. J. Refract. Met. Hard Mater.* 92 (2020), 105320, <https://doi.org/10.1016/j.ijrmhm.2020.105320>.
- [20] W.H. Haynes (Ed.), *CRC Handbook of Chemistry and Physics*, 95th ed., Taylor & Francis Group, Boca Raton (US), 2014.
- [21] A.A. Matei, I. Pencea, M. Branzei, D.E. Trancu, G. Țepeș, C.E. Sfetcu, E. Ciovică, A. I. Gherghilescu, G.A. Stanciu, Corrosion resistance appraisal of TiN, TiCN and TiAlN coatings deposited by CAE-PVD method on WC–Co cutting tools exposed to artificial sea water, *Appl. Surf. Sci.* 358 (2015) 572–578, <https://doi.org/10.1016/j.apsusc.2015.08.041>.

- [22] Z. Zhao, J. Liu, H. Tang, X. Ma, W. Zhao, Effect of Mo addition on the microstructure and properties of WC-Ni-Fe hard alloys, *J. Alloys Compd.* 646 (2015) 155–160, <https://doi.org/10.1016/j.jallcom.2015.05.277>.
- [23] P.K. Samal, J.W. Newkirk (Eds.), *ASM Handbook, Volume 7: Powder Metallurgy*, ASM International, Ohio (USA), 2015.
- [24] J.E. Cho, S.Y. Hwang, K.Y. Kim, Corrosion behavior of thermal sprayed WC cermet coatings having various metallic binders in strong acidic environment, *Surf. Coat. Technol.* 200 (2006) 2653–2662, <https://doi.org/10.1016/j.surfcoat.2004.10.142>.
- [25] C.M. Fernandes, V. Popovich, M. Matos, A.M.R. Senos, M.T. Vieira, Carbide phases formed in WC–M (M = Fe/Ni/Cr) systems, *Ceram. Int.* 35 (2009) 369–372, <https://doi.org/10.1016/j.ceramint.2007.11.001>.
- [26] S. Chen, W. Xiong, Z. Yao, G. Zhang, X. Chen, B. Huang, Q. Yang, Corrosion behavior of Ti(C,N)-Ni/Cr cermets in H₂SO₄ solution, *Int. J. Refract. Met. Hard Mater.* 47 (2014), <https://doi.org/10.1016/j.ijrmhm.2014.07.010>.
- [27] C.M. Fernandes, A. Rocha, J.P. Cardoso, A.C. Bastos, E. Soares, J. Sacramento, M.G. S. Ferreira, A.M.R. Senos, WC-stainless steel hardmetals, *Int. J. Refract. Met. Hard Mater.* 72 (2018) 21–26, <https://doi.org/10.1016/j.ijrmhm.2017.11.046>.
- [28] R. de Oro Calderon, A. Agna, U.U. Gomes, W.D. Schubert, Phase formation in cemented carbides prepared from WC and stainless steel powder – an experimental study combined with thermodynamic calculations, *Int. J. Refract. Met. Hard Mater.* 80 (2019) 225–237, <https://doi.org/10.1016/j.ijrmhm.2019.01.012>.
- [29] A.M.F. Rocha, A.C. Bastos, J.P. Cardoso, F. Rodrigues, C.M. Fernandes, E. Soares, J. Sacramento, A.M.R. Senos, M.G.S. Ferreira, Corrosion behaviour of WC hardmetals with nickel-based binders, *Corros. Sci.* 147 (2019) 384–393, <https://doi.org/10.1016/j.corsci.2018.11.015>.
- [30] Y. Peng, H. Miao, Z. Peng, Development of TiCN-based cermets: mechanical properties and wear mechanism, *Int. J. Refract. Met. Hard Mater.* 39 (2013) 78–89, <https://doi.org/10.1016/j.ijrmhm.2012.07.001>.
- [31] R.M. German, P. Suri, S.J. Park, Review: liquid phase sintering, *J. Mater. Sci.* 44 (2009) 1–39, <https://doi.org/10.1007/s10853-008-3008-0>.
- [32] P. Alvaredo, M. Dios, B. Ferrari, E. Gordo, Understanding of wetting and solubility behavior of Fe binder on Ti(C,N) cermets, *J. Alloys Compd.* 770 (2019) 17–25, <https://doi.org/10.1016/j.jallcom.2018.07.243>.
- [33] M. de Nicolás, H. Besharatloo, J.M. Wheeler, M. de Dios, P. Alvaredo, J.J. Roa, B. Ferrari, L. Llanes, E. Gordo, Influence of the processing route on the properties of Ti(C,N)-Fe₁₅Ni cermets, *Int. J. Refract. Met. Hard Mater.* 87 (2020), 105046, <https://doi.org/10.1016/j.ijrmhm.2019.105046>.
- [34] M. de Nicolás, H. Besharatloo, P. Alvaredo, J.J. Roa, L. Llanes, E. Gordo, Design of alternative binders for hard materials, *Int. J. Refract. Met. Hard Mater.* 87 (2020), 105089, <https://doi.org/10.1016/j.ijrmhm.2019.105089>.
- [35] V.A. Tracey, Nickel in hardmetals, *Int. J. Refract. Met. Hard Mater.* 11 (1992) 137–149, [https://doi.org/10.1016/0263-4368\(92\)90056-8](https://doi.org/10.1016/0263-4368(92)90056-8).
- [36] N. Eustathopoulos, M.G. Nicholas, B. Drevet (Eds.), *Wettability at high temperatures 3*, 1999, Pergamon, Oxford (UK).
- [37] P. Alvaredo, M. De Dios, B. Ferrari, E. Gordo, Interface study for the design of alternative matrixes in cermets, in: *Euro PM2015 Proc. Hard Mater. Altern. Bind.*, European Powder Metallurgy Association (EPMA), Shrewsbury (U.K.), 2015. ISBN: 978-1-899072-47-7.
- [38] E. Macía, Estudio de la Mojabilidad de Aleaciones de Fe Sobre Ti(C,N) Para el Diseño de Cermets, Master Thesis., Universidad Carlos III de Madrid, 2014.
- [39] P. Alvaredo, E. Macía, E. Gordo, Estudio de la intercara en materiales compuestos tipo cermet para el diseño de matrices metálicas alternativas, in: A. Ureña, J. Tortosa, J. Costa (Eds.), *Mater. Compuestos 15 Actas Del XI Congr. Nac. Mater. Compuestos*, Asociación Española de Materiales Compuestos (AEMAC), Móstoles Madrid, 2015, pp. 571–576.
- [40] P. Alvaredo, J.J. Roa, E. Jimenez-Pique, L. Llanes, E. Gordo, Characterization of interfaces between TiCN and iron-base binders, *Int. J. Refract. Met. Hard Mater.* 63 (2017) 32–37, <https://doi.org/10.1016/j.ijrmhm.2016.08.010>.
- [41] I. Konyashin, A.A. Zaitsev, D. Sidorenko, E.A. Levashov, B. Ries, S.N. Konischev, M. Sorokin, A.A. Mazilkin, M. Herrmann, A. Kaiser, Wettability of tungsten carbide by liquid binders in WC–Co cemented carbides: is it complete for all carbon contents? *Int. J. Refract. Met. Hard Mater.* 62 (2017) 134–148, <https://doi.org/10.1016/j.ijrmhm.2016.06.006>.
- [42] V.L. Silva, C.M. Fernandes, A.M.R. Senos, Copper wettability on tungsten carbide surfaces, *Ceram. Int.* 42 (2016) 1191–1196, <https://doi.org/10.1016/j.ceramint.2015.09.050>.
- [43] J. García, On the Formation of Graded Microstructures on Fe-Ni-Co Based Cemented Carbides and CVD Ti-C-N Coatings for Cutting Tools, Habilitation Thesis., Vienna University of Technology, 2013.
- [44] AENOR, Adhesives — Wettability — Determination by Measurement of Contact Angle and Surface Free Energy of Solid Surface, UNE-EN 828:2013, 2013.
- [45] ASTM International, Standard Practice for Surface Wettability of Coatings, Substrates and Pigments by Advancing Contact Angle Measurement, ASTM D7334-08, 2013, <https://doi.org/10.1520/D7334-08R13>.
- [46] Chapter 3: Methods of measuring wettability parameters — 3.1. Sessile drop experiments, in: N. Eustathopoulos, M.G. Nicholas, B. Drevet (Eds.), *Wettability High Temp.*, Elsevier Science, Oxford (UK), 1999, pp. 106–130. <https://books.google.es/books?id=T7I7IWVcGQC>.
- [47] U.S. Department of Commerce, Aluminum, Natl. Inst. Stand. Technol., 2021.
- [48] H.-O. Andrés, Microstructures of cemented carbides, *Mater. Des.* 22 (2001) 491–498, [https://doi.org/10.1016/S0261-3069\(01\)00006-1](https://doi.org/10.1016/S0261-3069(01)00006-1).
- [49] M. Walbrühl, D. Linder, J. Ågren, A. Borgenstam, Diffusion modeling in cemented carbides: solubility assessment for Co, Fe and Ni binder systems, *Int. J. Refract. Met. Hard Mater.* 68 (2017) 41–48, <https://doi.org/10.1016/j.ijrmhm.2017.06.006>.
- [50] D. Linder, Z. Hou, R. Xie, P. Hedström, V. Ström, E. Holmström, A. Borgenstam, A comparative study of microstructure and magnetic properties of a Ni–Fe cemented carbide: influence of carbon content, *Int. J. Refract. Met. Hard Mater.* 80 (2019) 181–187, <https://doi.org/10.1016/j.ijrmhm.2019.01.014>.
- [51] P. Alvaredo, E. Gordo, O. Van der Biest, K. Vanmeensel, Microstructural development and mechanical properties of iron based cermets processed by pressureless and spark plasma sintering, *Mater. Sci. Eng. A* 538 (2012) 28–34, <https://doi.org/10.1016/j.msea.2011.12.107>.
- [52] M. de Nicolás, H. Besharatloo, L. Pereira, A. Müller-Grunz, C. Bertalan, R. Ueseldinger, L. Llanes, E. Gordo, Ti(C,N)-Fe₁₅Ni₁₀Cr cermets as alternative hard materials: influence of the processing route and composition on their microstructure and properties, *Ceram. Int.* 47 (2021) 23318–23331, <https://doi.org/10.1016/j.ceramint.2021.05.045>.
- [53] M.A. Gren, G. Wahnström, Wetting of surfaces and grain boundaries in cemented carbides and the effect from local chemistry, *Materialia* 8 (2019), 100470, <https://doi.org/10.1016/j.mtla.2019.100470>.
- [54] C.M. Fernandes, A.M.R. Senos, M.T. Vieira, Control of eta carbide formation in tungsten carbide powders sputter-coated with (Fe/Ni/Cr), *Int. J. Refract. Met. Hard Mater.* 25 (2007) 310–317, <https://doi.org/10.1016/j.ijrmhm.2006.07.004>.
- [55] A. Soleimani-Gorgani, 14 - Inkjet Printing, in: J. Izdebska, S.B.T. Thomas (Eds.), *Print. Polym. – Fundam. Appl.*, William Andrew Publishing, 2016, pp. 231–246, <https://doi.org/10.1016/B978-0-323-37468-2.00014-2>.